



Sensitivity of multiangle, multispectral polarimetric remote sensing over open oceans to water-leaving radiance: Analyses of RSP data acquired during the MILAGRO campaign

Jacek Chowdhary^{a,b,*}, Brian Cairns^{a,b}, Fabien Waquet^c, Kirk Knobelspiesse^{a,b}, Matteo Ottaviani^b, Jens Redemann^d, Larry Travis^b, Michael Mishchenko^b

^a Department of Applied Physics and Applied Mathematics, Columbia University, 2880 Broadway, New York, NY 10025 USA

^b NASA Goddard Institute for Space Studies, 2880 Broadway, New York, NY 10025, USA

^c Laboratoire d'Optique Atmosphérique, Université des Sciences et Technologies de Lille, Villeneuve-d'Ascq, France

^d BAERI/NASA Ames Research Center, Moffett Field, CA 94035, USA

ARTICLE INFO

Article history:

Received 22 June 2010

Received in revised form 18 October 2011

Accepted 23 November 2011

Available online xxxx

Keywords:

Remote sensing

Polarization

RSP

MILAGRO

Aerosol

Hydrosol

Ocean color

Case-1 waters

Bio-optics

Chlorophyll *a*

CDOM

Plankton

Scattering

Radiative transfer

ABSTRACT

For remote sensing of aerosol over the ocean, there is a contribution from light scattered under water. The brightness and spectrum of this light depends on the biomass content of the ocean, such that variations in the color of the ocean can be observed even from space. Rayleigh scattering by pure sea water, and Rayleigh–Gans type scattering by plankton, causes this light to be polarized with a distinctive angular distribution. To study the contribution of this underwater light polarization to multiangle, multispectral observations of polarized reflectance over ocean, we previously developed a hydrosol model for use in underwater light scattering computations that produces realistic variations of the ocean color and the underwater light polarization signature of pure sea water. In this work we review this hydrosol model, include a correction for the spectrum of the particulate scattering coefficient and backscattering efficiency, and discuss its sensitivity to variations in colored dissolved organic matter (CDOM) and in the scattering function of marine particulates. We then apply this model to measurements of total and polarized reflectance that were acquired over open ocean during the MILAGRO field campaign by the airborne Research Scanning Polarimeter (RSP). Analyses show that our hydrosol model faithfully reproduces the water-leaving contributions to RSP reflectance, and that the sensitivity of these contributions to Chlorophyll *a* concentration [Chl] in the ocean varies with the azimuth, height, and wavelength of observations. We also show that the impact of variations in CDOM on the polarized reflectance observed by the RSP at low altitude is comparable to or much less than the standard error of this reflectance whereas their effects in total reflectance may be substantial (i.e. up to >30%). Finally, we extend our study of polarized reflectance variations with [Chl] and CDOM to include results for simulated spaceborne observations.

© 2011 Elsevier Inc. All rights reserved.

1. Introduction

The polarized intensity of light scattered by particles exhibits features as a function of wavelength and scattering angle that are distinctly different from those of the total scattered intensity (Coulson, 1988; Ulaby & Elachi, 1990; Videen et al., 2004). The polarized and total intensity features also exhibit very different sensitivities to particle properties such as size relative to the wavelength, shape, and composition (Hansen & Travis, 1974; Mishchenko et al., 2002). Furthermore, both sensitivities vary with particle properties. For example, the polarized component of light scattered by particles having a refractive index close to that of the surrounding medium, such as particulates suspended

in the ocean, shows fewer features with scattering angle and less variation with shape and size than the corresponding features of light scattered by particles that have a strong refractive-index contrast with the surrounding medium such as atmospheric aerosols. Finally, the features in polarized intensity of singly scattered light are much less likely to be washed out by those of multiply scattered light than is the case for the features in total intensity (Hansen & Travis, 1974; Hovenier et al., 2004; Mishchenko et al., 2006; van de Hulst, 1980). This is because the magnitude of polarized intensity of light scattered *n* times decreases rapidly with *n* as compared with the magnitude of total intensity. These differences cause the retrieval of aerosol properties from remotely sensed polarization to be much more accurate than the corresponding retrievals from remotely sensed intensity, as has been demonstrated in theoretical studies (Hasekamp & Landgraf, 2005; Mishchenko & Travis, 1997a, 1997b). Analyses of actual polarimetric remote sensing data obtained by the Polarization and Directionality of the Earth's

* Corresponding author. Tel.: +1 212 678 5643; fax: +1 212 678 5552.

E-mail address: jacek.chowdhary@nasa.gov (J. Chowdhary).

Reflectance (POLDER; Deschamps et al., 1994) instrument confirm these studies – whether these analyses focus exclusively on POLDER observations (e.g., Bréon & Goloub, 1998; Herman et al., 2005), or on a comparison of aerosol retrievals from POLDER and from intensity-only remote sensing such as from the moderate resolution imaging spectrometer (MODIS; Barnes et al., 1998) instrument (Gérard et al., 2005).

The recognition of the advantages of polarimetric remote sensing (Hansen & Travis, 1974; Hovenier et al., 2004; Mishchenko et al., 2004, 2006; Ulaby & Elachi, 1990; Videen et al., 2004) has led to the development of a new generation of satellite scanning instruments, such as the Aerosol Polarimetry Sensor (APS) instrument (Mishchenko et al., 2004, 2007; see specifications in Section 2), that combine, and in many respects surpass (except for cross ground-track swath), the polarimetric and multiangle measurement strengths of POLDER and the multispectral measurement strengths of MODIS. The launch of such instruments will lead to more accurate retrievals of aerosols as demonstrated by Chowdhary et al. (2001), but it also puts more stringent requirements on the modeling of remote sensing data. For example, Chowdhary et al. (2002, 2005) show that for remote sensing over oceans the polarization of light measured in the visible part of the spectrum yields valuable information about the complex refractive index of fine mode aerosols provided that the contributions of polarized water leaving radiance are appropriately dealt with. They demonstrate that such contributions become very small for principal plane observations and consequently limited their analyses to such viewing geometries. Similar arguments were made by Chami et al. (2001) and Harmel and Chami (2008), although it was argued there from analyses for a single wavelength in the visible that polarized water leaving radiance over open oceans can be ignored for most viewing geometries available from space borne observations.

To provide a lower boundary condition for aerosol retrievals from polarized reflectance observations outside the principal plane over open oceans, Chowdhary et al. (2006, henceforth referred to as C2006) developed a hydrosol model that reproduces empirically observed variations in ocean albedos as a function of biomass concentration in the ocean and of the wavelength of observation, and that provides the corresponding angular variation in intensity and polarization of water leaving radiance. The primary purpose of this hydrosol model is therefore not for retrieval of marine particulates but to account for oceanic contributions in polarimetric remote sensing of aerosols as in Hasekamp et al. (2011). Nevertheless, one can change the microphysical and bio-optical properties prescribed for such particles in this model to mimic local (natural) variations and anomalous cases. The objectives of this paper are 1) to revisit this model and assess changes caused by variations in colored dissolved organic matter (CDOM) and in the scattering matrix of marine particulates, 2) to validate the water-leaving total and polarized radiance computed with this model against actual data obtained from aircraft at various altitudes and azimuth angles, and 3) to assess the sensitivity of spaceborne polarimetry over open oceans to variations in polarized water-leaving radiance. The organization of this paper is as follows. Section 2 provides a description of the airborne polarization data analyzed in this work, and of the field campaign in which these data were obtained. In Section 3, we evaluate the hydrosol model used in the analysis of underwater-light contributions to these data. The multiple scattering computations that link the hydrosol model to the polarization data are briefly reviewed in Section 4. Section 5 applies these computations to sensitivity studies of underwater light scattering, to analyses of the airborne polarization data, and to simulations of spaceborne polarization data. Finally, we summarize our results in Section 6.

2. Measurements

The primary measurements used in this work are obtained by the Research Scanning Polarimeter (RSP) instrument (Cairns

et al., 1999), which is an airborne version of the APS satellite instrument (Peralta et al., 2007). The objectives of APS-like measurements are discussed and detailed in Mishchenko et al. (2007), and can be summarized as the retrieval of the optical thickness, size distribution, complex refractive index, and shape information for fine and coarse mode aerosols, as well as of the size distribution and optical thickness of ice and water clouds, with very high accuracies in order to study and help quantify aerosol direct and indirect climate effects. To achieve high accuracy in the retrieved properties of aerosols requires measuring the spectral and angular variation of both the total and the polarized intensity of sunlight reflected by the Earth. APS-like instruments accomplish this by viewing each pixel along its ground track from 255 angles covering an angular range of $+60^\circ/-70^\circ$ with respect to nadir. For each angle the Stokes parameters I , Q , and U are measured simultaneously at 9 narrow-band wavelengths, λ , in the visible and short-wave near-infrared ($\lambda = 410, 443, 550, 670, 865, 910, 1378, 1610$, and 2200 nm) with an accuracy in degree of linear polarization of $\leq 0.2\%$. The instantaneous field-of-view (IFOV) for the APS was 8 mrad, which at a nominal altitude of 705 km leads to a nadir-viewing pixel size of 5.6 km. The RSP measurements are similar to those of the APS except for viewing the Earth from 152 angles instead of 255, with IFOV = 14 mrad instead of 8 mrad, and at $\lambda = 470, 960, 1590, 1880$, and 2250 nm instead of $\lambda = 443, 910, 1610, 1378$, and 2200 nm, respectively (Cairns et al., 1999). Note that both the 1880 and 1378 nm bands are extremely effective for screening thin cirrus clouds, but the 1378 nm band on the APS instrument allows for better detection and characterizing of stratospheric aerosols in case of a major volcanic eruption (Cairns et al., 2009).

The RSP data analyzed here were collected during phase B of the NASA-sponsored field experiment called the Intercontinental Chemical Transport Experiment (INTEX). The INTEX objectives were to study the transport and evolution of trace gases and aerosols on trans- and inter-continental scales, and to assess their impact on air quality and climate. The INTEX-B field study was coordinated with other agencies as part of the Megacity Initiative: Local and Global Research Observations (MILAGRO) campaign, which focused on the flow of pollution out of Mexico City during the month of March 2006. An overview of this campaign – including a summary of the instruments deployed and a discussion of more than 120 papers resulting from the INTEX-B field study – is given by Molina et al. (2010). Thirteen successful flights were carried out over and downwind of Mexico City by the Sky Research Inc. Jetstream 31 aircraft (J31, see upper right corner of Fig. 1) to study aerosol, water vapor, cloud, and surface properties. The instrument payload carried by the J31 included the RSP, the 14-channel NASA Ames Airborne Tracking Sun-photometer (AATS-14) which tracks the sun and measures direct solar beam transmission at 14 discrete wavelengths from 353 to 2139 nm (Redemann et al., 2009), and the Solar Spectral Flux Radiometer (SSFR) which is a moderate resolution spectrometer covering the spectral range of 350–2100 nm (Bergstrom et al., 2010). Cairns et al. (2009) describe the retrieval of aerosols over land from RSP observations obtained on 15 March 2006, and Knobelspiesse et al. (2011) discuss the retrieval of aerosols above clouds from RSP observations obtained on 13 March 2006. Here, we focus on RSP data obtained on 10 March 2006. This day is the first out of a set of three (partially) cloud-free days (i.e., 10, 13, and 18 March) during which the J31 flew over a patch of the Gulf of Mexico identified in SeaWiFS and MODIS/Aqua satellite imagery as case 1 ocean waters, i.e., oceanic waters whose optical properties are dominated by phytoplankton and their by-products. It is further the only day out of these three days during which the J31 flew at low- and mid-altitudes and for each of these altitudes at relative azimuth angles close to and far from the solar principal plane (see Fig. 1 for summary).

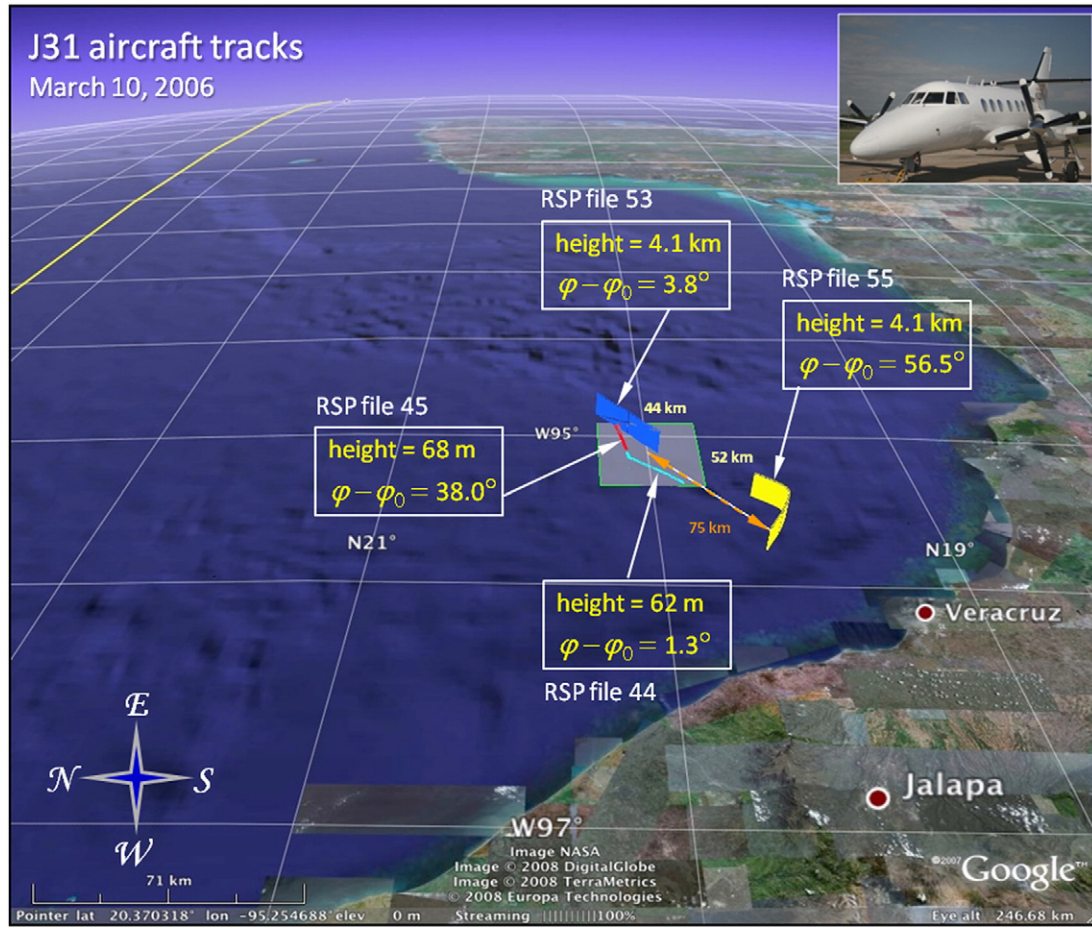


Fig. 1. Flight tracks, altitudes, and relative azimuth angles of RSP reflectance files collected during MILAGRO/INTEX-B that are analyzed in the current work.

3. Hydrosol model

3.1. Bulk ocean

To compute the scattering matrix and single scattering albedo of ocean waters, we consider these waters to be a bulk mixture of sea-water, with scattering matrix \mathbf{F}_w and scattering coefficient b_w , and a particulate component, with scattering matrix \mathbf{F}_p and scattering coefficient b_p (see Table 1 for notation, dimension, and definition of variables). We follow the convention that a scattering matrix \mathbf{F} has its scattering function referred to using the italic font face, i.e. $F \equiv \mathbf{F}_{11}$ (C2006), and the scattering function satisfies the normalization condition

$$\int_{4\pi} F(\Theta) \frac{d\Omega}{4\pi} = 1 \quad (1)$$

where Θ is the scattering angle and $d\Omega$ is the element of a solid angle. Note that our normalization differs by a factor of $(4\pi)^{-1}$ from that commonly adopted by the ocean color community. The scattering matrix \mathbf{F}_{blk} for a bulk ocean mixture can now be written as

$$\mathbf{F}_{\text{blk}}(\lambda, \Theta) = \frac{b_w(\lambda)\mathbf{F}_w(\Theta) + b_p(\lambda)\mathbf{F}_p(\Theta)}{b_w(\lambda) + b_p(\lambda)} \quad (2)$$

where \mathbf{F}_p is assumed to be independent of λ . Note that Eq. (2) ignores inelastic scattering, the ramifications of which are discussed by C2006. Following Morel (1974) we use the Rayleigh scattering law

with a depolarization factor of 0.09 to compute scattering matrix \mathbf{F}_w (Hansen & Travis, 1974), while for the scattering coefficient b_w we use the values of Smith and Baker (1981). Similarly, we write for the single scattering albedo ω_{blk} of our bulk ocean mixture

$$\omega_{\text{blk}}(\lambda) = \frac{b_w(\lambda) + b_p(\lambda)}{b_w(\lambda) + b_p(\lambda) + a_{\text{blk}}(\lambda)} \quad (3)$$

where a_{blk} is the bulk ocean absorption coefficient. In other words, a_{blk} is the sum of the absorption coefficients for pure seawater, marine particulates, and CDOM (also known as “yellow substance”).

The scattering matrix \mathbf{F}_p and coefficient b_p in Eq. (2) can be computed from the size distribution, refractive index, and abundance of marine particulates using the Mie theory for spherical particles or the T -matrix method (Mishchenko et al., 2000) for non-spherical particles. However, the resulting amount of light scattered backwards is often inconsistent with that obtained from in situ measurements in open oceans (Stramski & Kiefer, 1991; Stramski et al., 2004). Among the causes of this disagreement are large uncertainties in the micro-physical properties (size distribution, shape, and bulk refractive index as well as internal structure) of marine particulates. Another reason is the variation of the particulate scattering function F_p with plankton concentration derived from these measurements, which implies that there must be several types of marine particulates whose concentrations co-vary with that of plankton. Similar problems are encountered when computing the absorption coefficient a_{blk} in Eq. (2) from the physical properties and abundance of ocean water constituents. The absorption properties of CDOM are particularly

Table 1
Symbols, units and definitions of variables.

Symbol	Units	Definition
A_{blk}^a	(unitless)	Ratio of upward irradiance E_u and downward irradiance E_d for bulk oceanic waters, measured just below the ocean surface: $A_{\text{blk}} \equiv E_u/E_d$
$a_{\text{blk}}, a_p, a_w, a_y$	m^{-1}	Absorption coefficient for bulk oceanic waters, and for their particulate matter, pure seawater, and yellow substance (CDOM) components, respectively – see Eq. (22)
b_p, b_w	m^{-1}	Scattering coefficient for the particulate matter and pure seawater components of bulk oceanic waters, respectively
[Chl]	mg m^{-3}	Chlorophyll <i>a</i> concentration
$\Delta\varphi$	degrees	Difference between viewing azimuth angle φ and solar azimuth angle φ_0 : $\Delta\varphi \equiv \varphi - \varphi_0$
$d\Omega$	sr	Infinitesimal element of solid angle
ε	(unitless)	Combined standard error for RSP reflectance: $\varepsilon \equiv \sqrt{(\kappa^2 + \xi^2)}$
ζ	(unitless)	Calibration uncertainty (assumed to be 3.5%) ^d for RSP reflectance ρ_{tot} or ρ_{pol}
η	(unitless)	Polarization uncertainty (assumed to be 0.002) for RSP reflectance ratio $\rho_{\text{pol}}/\rho_{\text{tot}}$
γ	(unitless)	Exponent for Junge-type differential size distribution
\mathbf{F}	(unitless)	Scattering matrix (4×4) for scattering matter volume elements
$\mathbf{F}_{\text{blk}}, \mathbf{F}_p, \mathbf{F}_w$	(unitless)	Scattering matrix (4×4) for bulk oceanic water volume elements, and for their particulate matter and pure seawater components, respectively – see Eq. (2)
F, F_p	(unitless)	The (1,1) elements (i.e., scattering functions) of matrices \mathbf{F} and \mathbf{F}_p , respectively
f_{det}	(unitless)	Number fraction of marine particulates that are detritus – see Eq. (16)
g_p	(unitless)	Asymmetry parameter for scattering function F_p : $g_p \equiv \int F_p(\theta) \cos(\theta) d\theta$
θ	degree	Single scattering angle
θ_0, θ	degree	Solar zenith angle and viewing nadir angle, respectively
I, Q, U	W m^{-2}	First, second, and third parameter of a Stokes vector, respectively
$K_{\text{blk}}, K_{\text{bio}}, K_w$	m^{-1}	Diffuse downward irradiance attenuation coefficient for bulk oceanic waters, and for their biogenic and pure seawater components, respectively – see Eq. (8)
κ	(unitless)	Measurement uncertainty for RSP reflectance: $\kappa \equiv \sqrt{(\{\zeta \times \rho_{\text{pol}}\}^2 + \{\eta \times \rho_{\text{tot}}\}^2)}$ for ρ_{pol}
λ	nm	Wavelength of light
m	(unitless)	Complex refractive index of marine particles, relative to pure seawater
μ_0, μ	(unitless)	Cosine of angles θ_0 and θ , respectively: $\mu_0 \equiv \cos(\theta_0)$ and $\mu \equiv \cos(\theta)$
μ_d, μ_u	(unitless)	Average cosine of downward and upward flux of light in oceanic waters, respectively
ξ	(unitless)	Scan-to-scan standard error for RSP reflectance
q_p, q_w	(unitless)	Backscattering efficiency of scattering functions F_p and F_w , respectively – see Eq. (13) for q_p
$\rho_{\text{tot}}, \rho_{\text{pol}}$	(unitless)	Total RSP reflectance and polarized RSP reflectance, respectively – see Eqs. (25)–(26)
ρ_{max}, S_0	(unitless) W m^{-2}	Maximum value of reflectance ρ_{tot} or ρ_{pol} Extraterrestrial solar flux
S_{blk}^c	m^{-1}	Backscattering coefficient of bulk oceanic water – see Eq. (12)
$\sigma_{\text{det}}, \sigma_{\text{plk}}$	μm^2	Scattering cross sections of detritus particles and plankton particles, respectively
$\tau_{\text{fine}}, \tau_{\text{coarse}}$	(unitless)	Optical thickness of fine mode aerosol and coarse mode aerosol, respectively
φ_0, φ	degrees	Solar and viewing azimuth angle, respectively
ω_{blk}	(unitless)	Single scattering albedo for bulk oceanic waters
z	m	Altitude with respect to sea level

^a R in the notation of Morel and Maritorena (2001).

^b b_{bp} in the notation of Morel and Maritorena (2001).

^c b_b in the notation of Morel and Maritorena (2001).

^d Fig. 13 considers also the case of $\zeta = 1.5\%$ and 3% .

difficult to predict because the interactions between light and the compounds that make up the optically-active organic substances of CDOM are difficult to assess, and because the local (photo-) chemical and biological processes that create and alter these compounds are not well known (Nelson & Siegel, 2002, and references therein). Adding to

this problem is that CDOM is usually measured as the collective of substances that pass through a submicron filter. Hence, CDOM may not only consist of dissolved organic materials but also of marine particulates that are smaller than a few tenths of a micrometer and collectively defined as colloids (Stramski & Woźniak, 2005). Nonetheless the contribution of absorption by CDOM to a_{blk} cannot be ignored. Indeed, comparisons of empirical relationships for open ocean absorption spectra show that this contribution dominates the non-water absorption component of a_{blk} for blue and red wavelengths except when the ocean is extremely oligotrophic (Morel, 2009). Furthermore, deviations of ocean color from established global mean trends are highly correlated with anomalies in CDOM (Brown et al., 2008; Morel et al., 2007).

To address these problems, we follow the approach described in C2006. This approach uses the bio-optical model for case 1 waters developed by Morel and Maritorena (2001), and an upper bound for various measurements of underwater light polarization signatures (e.g., Voss & Fry, 1984), to constrain a_{blk} and both the samples and mixtures of two classes of marine particulates: detritus and plankton, henceforth referred to as D–P mixtures. The class of detrital particles follows the definition used by Siegel et al. (2002) and stands for the entire spectrum of non-plankton particles, i.e., it covers a wide range of particles including those of biogenic origin with high refractive indices such as skeletal and shell remains (Stramski & Kiefer, 1991). It may for open oceans even include non-biogenic high-refractive particles such as minerals from aeolian input (Twardowski et al., 2001). However, our D–P model is not expected to be valid for cases where the amount of dust is large enough to cause significant changes in the color of the ocean (Claustre et al., 2002; Woźniak & Stramski, 2004) and probably also in the polarization of underwater light (Chowdhary et al., 2005). The bio-optical and mixing equations for the resulting D–P mixtures are briefly reviewed here for two reasons. Firstly, they include some corrections to the bio-optical model that we used previously (C2006). The ramifications of these corrections for water-leaving radiance are discussed in more detail in Appendix A. Secondly, the corrected bio-optical model will be compared in Section 5 with a different bio-optical approximation for absorption by CDOM as part of a discussion of the sensitivity of ocean color to variations in the scattering matrix of marine particulates and absorption by CDOM.

3.2. Bio-optical model

The particulate scattering coefficient b_p in Eqs. (2) and (3) is obtained from the empirical relationship derived by Loisel and Morel (1998) for the upper homogeneous layer of an open ocean at $\lambda = 660$ nm:

$$b_p^{660} \equiv b_p(\lambda = 660) = 0.347[\text{Chl}]^{0.766}, \quad (4)$$

where [Chl] is the concentration of Chlorophyll *a*, a photosynthetic pigment found in plankton. Morel and Maritorena (2001) discuss the spectral variation of this coefficient, and argue that it should increase with the relative amount of small, non-absorbing detritus particles from being spectrally flat to having a λ^{-1} dependence. Such variations in spectra were recently measured by Huot et al. (2008) along an 8000 km transect of the South Pacific Gyre, and found to agree well over the [Chl] range from 0.02 to 2.0 mg/m³ and at $\lambda = 420, 470$, and 550 nm with the following equation:

$$b_p(\lambda) = b_p^{660} \left(\frac{660}{\lambda} \right)^k, \quad (5)$$

with

$$k = \begin{cases} 0.5(\log_{10}[\text{Chl}] - 0.3), & 0.02 \leq [\text{Chl}] \leq 2 \text{ mgm}^{-3}, \\ 0, & [\text{Chl}] > 2 \text{ mgm}^{-3}. \end{cases} \quad (6)$$

Note that this spectrum differs from the λ^{-1} dependence of b_p for all [Chl] that we previously used (C2006). In this work we adopt Eqs. (4)–(6) for b_p and list its values in Table 2 as a function of [Chl] for $\lambda = 410$ and 550 nm.

To obtain the bulk ocean absorption coefficient a_{blk} in Eq. (3), we follow Morel and Maritorena (2001) who compute a_{blk} from the bulk downward irradiance attenuation coefficient K_{blk} and the ratio A_{blk} of the bulk downward and upward irradiance just below the ocean surface, viz,

$$a_{\text{blk}}(\lambda) = K_{\text{blk}}(\lambda) \{1 - A_{\text{blk}}(\lambda)\} \frac{\mu_d \mu_u}{\mu_d A_{\text{blk}}(\lambda) + \mu_u} \quad (7)$$

where μ_d and μ_u are the average cosine directions for the downward and upward underwater light flux, respectively. The advantage of using this equation to retrieve a_{blk} is that K_{blk} , and hence anything retrieved from it, necessarily incorporates the absorption by all matter including CDOM. From Morel and Maritorena (2001), we express K_{blk} as the sum of its components

$$K_{\text{blk}}(\lambda) = K_w(\lambda) + K_{\text{bio}}(\lambda) \quad (8)$$

where the contribution to the attenuation coefficient from water is approximated by

$$K_w(\lambda) = a_w(\lambda) + 0.5b_w(\lambda) \quad (9)$$

and the contribution to the attenuation coefficient from all other scattering and absorbing (particulate and dissolved) matter is

$$K_{\text{bio}}(\lambda) = \chi(\lambda)[\text{Chl}]^{e(\lambda)}. \quad (10)$$

The contribution to the attenuation coefficient from particulate and dissolved matter, K_{bio} , is derived empirically by regressing log-transformed values of $(K_{\text{blk}} - K_w)$ against [Chl] with $\chi(\lambda)$ and $e(\lambda)$ being the regression coefficients. To evaluate K_{blk} , we use for a_w the values from Pope and Fry (1997), and for $\chi(\lambda)$ and $e(\lambda)$ the values from Morel and Maritorena (2001). The irradiance ratio A_{blk} is determined from the expression (Gordon et al., 1975; Morel & Prieur, 1977),

$$A_{\text{blk}}(\lambda) = \alpha(\lambda) \frac{s_{\text{blk}}(\lambda)}{a_{\text{blk}}(\lambda)} \quad (11)$$

where α is a dimensionless pre-factor which has a value of ~ 0.3 for oligotrophic waters and clear blue skies with the sun overhead, and where s_{blk} is the bulk ocean backscattering coefficient. Variations of

α with decreasing solar zenith angle θ_0 and with increasing [Chl] and λ are given by Morel and Gentili (1991) and by Morel et al. (2002). The backscattering coefficient s_{blk} is defined as

$$s_{\text{blk}}(\lambda) \equiv q_w b_w(\lambda) + q_p b_p(\lambda) \quad (12)$$

where

$$q_p \equiv 2\pi \int_{0.5\pi}^{\pi} \frac{F_p(\Theta)}{4\pi} \sin(\Theta) d\Theta \quad (13)$$

is the particulate backscattering efficiency using the normalization convention of Eq. (1), and similarly for q_w . We remark that $q_w \approx 0.5$ for Rayleigh scattering with small depolarization factors. Morel (1988) parameterized q_p as a function of λ and [Chl] based on theoretical considerations and in situ measurements, and Morel and Maritorena (2001) refined that parameterization to better represent strongly oligotrophic cases. The final form of the parameterization, shown by Huot et al. (2008) who also validated it using in situ data from the South Pacific Gyre, is

$$q_p = 0.002 + 0.01\{0.50 - 0.25 \log_{10}[\text{Chl}]\}. \quad (14)$$

Note that this relation does not contain the λ^{-k} wavelength dependency of Eq. (5) that was used by us in C2006, i.e. the particulate backscattering efficiency is now considered to be spectrally invariant. In this work we adopt Eq. (14) for q_p and list its values in Table 2 as a function of [Chl]. Substituting for K_{blk} the empirical relation derived from Eqs. (8)–(10), and for s_{blk} the empirical relation derived from Eqs. (4), (12) and (14), we reduce the unknown terms in Eqs. (7) and (11) to A_{blk} , a_{blk} , μ_d and μ_u for a given [Chl]. Adopting further for μ_d and μ_u the values tabulated by Morel and Maritorena (2001), we solve Eqs. (7) and (11) simultaneously to obtain A_{blk} and a_{blk} as a function of [Chl]. The results for a_{blk} at $\lambda = 410$ and 550 nm are listed in Table 2 as a function of [Chl], and we use these absorption coefficients to compute the bulk ocean single scattering albedo ω_{blk} in Eq. (3) except when noted otherwise.

For our retrieval of a_{blk} , we remark that Morel and Maritorena (2001) assume for their μ_d and μ_u values a solar zenith angle θ_0 of 30° and an ocean thickness limited to (approximately) the first penetration depth of light in sea as defined in Gordon and McCluney (1975). These assumptions replicate the average conditions for their K_{bio} measurements (see also Morel & Gentili, 2004), and require for α in Eq. (11) that the same solar zenith angle be adopted. As a result, the values of A_{blk} retrieved from Eq. (11) are valid only for $\theta_0 = 30^\circ$. However, a_{blk} is an inherent optical property (i.e., it does not vary with the ambient light field) and its retrieved values in Table 2 are therefore valid for all θ_0 . To verify this, we consider the following approximation by Gordon (1989):

$$\mu_{d,z=0} \times K_{\text{blk},z=0}(\lambda) \approx 1.0395\{a_{\text{blk}}(\lambda) + s_{\text{blk}}(\lambda)\}. \quad (15)$$

Here, $\mu_{d,z=0}$ and $K_{\text{blk},z=0}$ are the respective values of μ_d and K_{blk} evaluated for an infinitesimally thin ocean layer just below the ocean surface. Eq. (15) implies that the product of $\mu_{d,z=0}$ and $K_{\text{blk},z=0}$ does not vary with θ_0 , and that it can be used to estimate a_{blk} for given s_{blk} . Substituting Eq. (12) for s_{blk} , and approximating $\mu_{d,z=0}$ and $K_{\text{blk},z=0}$ with the μ_d and K_{blk} values from Morel and Maritorena (2001), we obtain a_{blk} values that are within 4% of those listed in Table 2. In fact, the agreement remains good for the entire range of $0.03 \text{ mg/m}^3 \leq [\text{Chl}] \leq 3.0 \text{ mg/m}^3$ and $400 \text{ nm} \leq \lambda \leq 700 \text{ nm}$ (compare solid and short-dash curves in Fig. 3b).

Table 2

Bio-optical scattering and absorption properties for Case 1 waters as a function of [Chl], and the corresponding parameters for the D–P (DP), the one term Henyey–Greenstein (OTHG) and the Fourmieri–Forand (FF) bulk ocean scattering functions shown in Fig. 2.

[Chl] ^a	0.03	0.10	0.30	1.00	3.00
q_p	0.0108	0.0095	0.0083	0.0070	0.0058
$b_p(410 \text{ nm})^b$	0.0365	0.0810	0.1678	0.3727	0.8050
$b_p(550 \text{ nm})^b$	0.0279	0.0670	0.1487	0.3566	0.8050
$a_{\text{blk}}(410 \text{ nm})^b$	0.0121	0.0233	0.0448	0.0951	0.1922
$a_{\text{blk}}(550 \text{ nm})^b$	0.0530	0.0567	0.0633	0.0779	0.1065
$f_{\text{det}}(\text{DP})$	0.61	0.56	0.50	0.43	0.34
$m(\text{FF})$	1.08455	1.08120	1.07780	1.07375	1.06955
$g_p(\text{OTHG})$	0.95038	0.95610	0.96145	0.96729	0.97275

^a In mg/m^3 .

^b In m^{-1} .

3.3. Detritus–plankton mixtures

The bio-optical equations given in the previous section describe amongst others variations of the particulate backscattering efficiency q_p with [Chl]. These variations can only originate from corresponding changes in the particulate scattering function F_p of scattering matrix \mathbf{F}_p . To emulate such changes in F_p , we consider mixtures of detritus and plankton particles. The particulate scattering matrix for such a D–P mixture becomes

$$\mathbf{F}_p(\Theta) = \frac{\{1-f_{\text{det}}\}\sigma_{\text{plk}}\mathbf{F}_{\text{plk}}(\Theta) + f_{\text{det}}\sigma_{\text{det}}\mathbf{F}_{\text{det}}(\Theta)}{\{1-f_{\text{det}}\}\sigma_{\text{plk}} + f_{\text{det}}\sigma_{\text{det}}} \quad (16)$$

where f_{det} is the fraction of the total number of particles that are detritus, \mathbf{F}_{plk} and \mathbf{F}_{det} are the scattering matrices and σ_{plk} and σ_{det} are the scattering cross sections for the plankton and detritus particles, respectively. Note for q_p that this leads to

$$q_p = \frac{\{1-f_{\text{det}}\}\sigma_{\text{plk}}q_{\text{plk}} + f_{\text{det}}\sigma_{\text{det}}q_{\text{det}}}{\{1-f_{\text{det}}\}\sigma_{\text{plk}} + f_{\text{det}}\sigma_{\text{det}}} \quad (17)$$

where q_{plk} and q_{det} are the backscattering efficiencies defined similarly to q_p in Eq. (13) except for the scattering functions F_{plk} and F_{det} , respectively. Changes in F_p that are consistent with the bio-optical variations of q_p can then be obtained by varying f_{det} with [Chl] to match Eqs. (14) and (17) for given sets of $\{\sigma_{\text{plk}}, q_{\text{plk}}\}$ and $\{\sigma_{\text{det}}, q_{\text{det}}\}$.

Following C2006, we use the bimodality observed for the refractive index m of marine particulates (Zaneveld et al., 1974) to define our plankton and detritus classes. We assign to each refractive index for these classes a Junge-type differential size distribution, and constrain its Junge exponent γ by requiring the corresponding scattering matrix to produce the same linear polarization properties as \mathbf{F}_w . This leads to

$$\gamma = 6.63m - 3.25(\pm 0.05) \begin{cases} 1.03 \leq m \leq 1.06, & \text{plankton;} \\ 1.15 \leq m \leq 1.25, & \text{detritus,} \end{cases} \quad (18)$$

under the assumption that the particles are spherical and homogeneous. Clearly, the non-living low-refractive particles are not part of the detritus matter in this classification; in fact, they are more akin to the plankton matter. Also, the assumption of spherical geometry and homogeneity is not true for most oceanic particulates. However, the prime objective of the D–P mixtures is to reproduce the bidirectional distribution of radiance and polarization emerging from the ocean, not to provide an accurate diagnostic model of the contributions to what is observed. This is similar to the objective of atmospheric correction in the remote sensing of ocean color, which is to account for the contribution of atmospheric scattering to the observed signal rather than diagnose what generated the signal. We refer to C2006 for a more detailed discussion of these assumptions.

In this work, we choose the D–P mixture with the same members of detritus and plankton classes as in C2006. The Junge exponent γ and refractive index m of these members are given in Table 3 together with the resulting scattering cross section σ and backscattering ratio q . The corresponding values of f_{det} are listed as a function of [Chl] in Table 2, and are well represented by the polynomial fit

$$f_{\text{det}}(\text{Chl}) = 0.61 - 0.099(x_{\text{Chl}}) - 0.009(x_{\text{Chl}})^3 (\pm 3 \times 10^{-3}) \quad (19)$$

where

$$x_{\text{Chl}} = \log_{10} \frac{[\text{Chl}]}{0.03}. \quad (20)$$

Note that this variation differs from that previously presented (C2006) because of the correction we made to the particulate backscattering efficiency which now has no spectral variation. The bulk ocean

Table 3

Properties of the plankton and detritus components of a D–P hydrosol mixture.

Properties	Plankton	Detritus
Junge size distribution exponent γ : ^a	3.7	4.4
Real refractive index m :	1.04	1.15
Scattering cross section σ : ^b	8.874×10^{-5}	1.388×10^{-5}
Backscattering efficiency q :	2.663×10^{-3}	4.444×10^{-2}

^a Assuming spherical particles with radii between 0.01 and 100 μm .

^b In μm^2 .

scattering functions F_{blk} , normalized by 4π , for this D–P mixture are shown in Fig. 2 ('DP' curves) for $\lambda = 410$ nm and 550 nm (left and right panel) as a function of [Chl]. For future reference (see Sections 5.1 and 5.2), we also include in this figure the corresponding results for Fournier–Forand scattering functions ('FF' curves), for scattering functions of 'typical' plankton-only particles ('Plankton' curves), and for one-term Henyey–Greenstein scattering functions ('OTHG' curves).

4. Multiple-scattering computations

The total and polarized reflectance of radiation emerging from the top of an atmosphere–ocean system (AOS) are calculated as in C2006, where various numerical recipes used to increase the efficiency of computations are described. That is, we first use the doubling/adding method for radiative transfer computations of polarized light (de Haan et al., 1987; Hovenier et al., 2004) to obtain the reflection and transmission properties of the atmosphere and the ocean body, and the geometric-optics approach to obtain the reflection and transmission properties of a wind-ruffled ocean surface. We then compute from these properties the reflection matrix of the combined AOS by adding the three AOS components together. To obtain the upwelling radiation field inside the atmosphere measured from an aircraft, we first apply the same sequence of methods for the partial AOS below the aircraft. The internal radiation field just below the aircraft is then rendered as a byproduct by using the adding method to subsequently add the atmospheric layer above the aircraft to the partial AOS. A recent comparison with an independently written radiative transfer code (Zhai et al., 2010) resulted in a very good agreement (relative difference $\leq 0.1\%$) for Stokes parameters I , Q and U of water-leaving radiance.

The AOS used in these computations is specified as follows. The atmosphere is divided into two main layers: a purely molecular layer (including ozone) for altitudes above 4 km (i.e., above the aircraft) and a layer consisting of a homogeneous mixture of gas (including water vapor) and aerosol particles for altitudes below 4 km down to 65 m. The lowest 65 m may contain a thin haze of water droplets in addition to the aerosol particles of the lower atmosphere. We assume the aerosol to be bimodal and allow the complex refractive index and its spectrum, the size distribution, the particle shape, and the optical thickness of one mode to be independent of those of the other mode. For the scattering of diffuse light and reflection of attenuated sun light by the ocean surface we adopt the wind-speed and wind-direction dependent slope distribution measured by Cox and Munk (1954), and include shadowing effects (Sancer, 1969) as well as scattering by oceanic foam (Frouin et al., 1996; Koepke, 1984). The ocean body is assumed to be a homogeneous mixture between pure seawater and particulates (Section 3.1). Except when noted otherwise, we use for the inherent optical properties of this mixture the scattering and absorption coefficients listed in Table 2 (see discussion in Section 3.2), and the D–P particulates specified in Table 3 (see discussion in Section 3.3). The ocean body optical thickness is fixed at 20, and we ignore the presence of an ocean bottom.

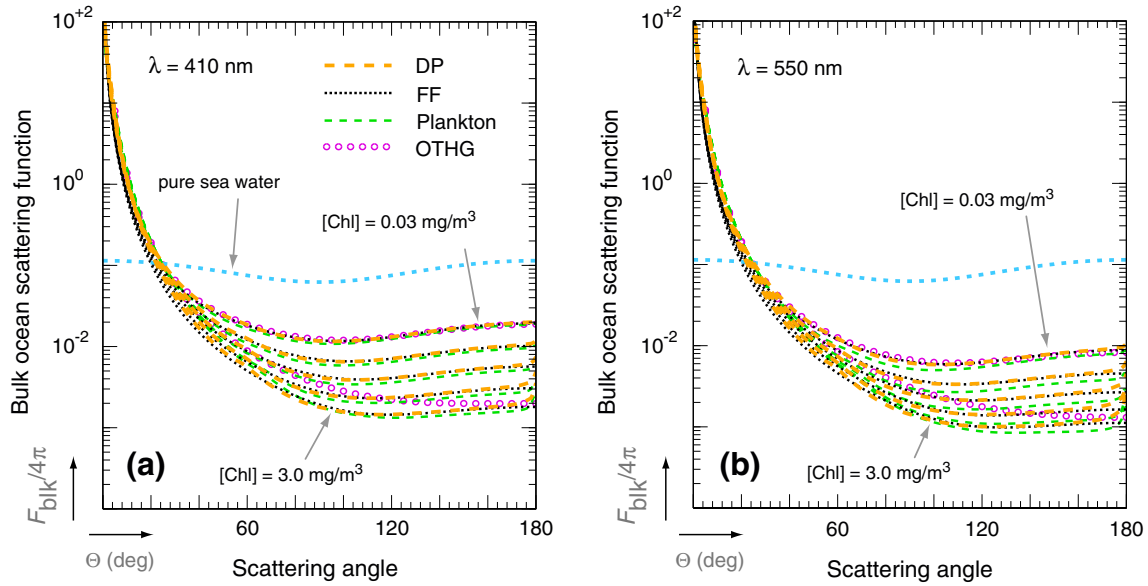


Fig. 2. (a) Bulk ocean scattering functions F_{blik} as a function of scattering angle θ and Chlorophyll a concentration $[\text{Chl}]$. The functions are normalized as in Eq. (1), and the mixing between water and particulates occurs according to Eq. (2) with scattering coefficients b_p taken from Table 2. The wavelength λ is 410 nm, and $[\text{Chl}] = 0.03, 0.1, 0.3, 1.0$ and 3.0 mg/m^3 . The unlabeled scattering functions F_{blik} decrease monotone in the backscattering direction with increasing $[\text{Chl}]$. Yellow-dash curve ('DP'): F_{blik} results for marine particulate consisting of plankton and matter specified in Table 1 with f_{det} varied as in Table 2. Black-dot curve ('FF'): F_{blik} results for Fournier–Forand particulate scattering functions obtained from Mobley et al. (2002) with refractive index m varied as in Table 2. Green-dash curve ('Plankton'): F_{blik} results for the 'typical' plankton matter discussed in Section 5.1. Open circles ('OTHG'): F_{blik} results (shown only for $[\text{Chl}] = 0.03$ and 3.0 mg/m^3) for one term Henyey–Greenstein particulate scattering functions with asymmetry parameter g_p varied as in Table 2. Shown also (cyan-dash curve) is the scattering function F_w for pure sea water. (b) Same as in Fig. 2a except for wavelength $\lambda = 550 \text{ nm}$. (For interpretation of the color references in this figure legend, the reader is referred to the web version of this article).

5. Results and discussion

5.1. Irradiance ratio sensitivity analysis

The graphs in Fig. 3a depict model variations of the bulk ocean irradiance ratio A_{blik} , and in Fig. 3b of the bulk ocean absorption coefficient a_{blik} , with wavelength λ for various concentrations of Chlorophyll a . The spectral range evaluated is from 400 to 700 nm which covers those spectral bands used for aerosol remote sensing by RSP and APS-like instruments, and also the spectral bands typically used for remote sensing of ocean color (Esaias et al., 1998). Note

however that our models do not account for fluorescence by Chlorophyll a that would have led to a distinctive peak in A_{blik} at $\lambda \approx 685 \text{ nm}$. The chlorophyll a concentration range of 0.03 mg/m^3 to 3.0 mg/m^3 , encompasses typical values found in open oceans except for cases of extreme plankton blooms. The atmosphere is assumed to be purely molecular, the wind speed is 7 m/s, and the solar zenith angle θ_0 is 30° . The colored solid curves in Fig. 3a are the semi-analytical spectra of A_{blik} from the bio-optical model discussed in Section 3.2. The colored circles in this figure show corresponding radiative transfer (RT) results in which F_p is provided by the D–P model discussed in Section 3.3. Excellent agreement can be observed

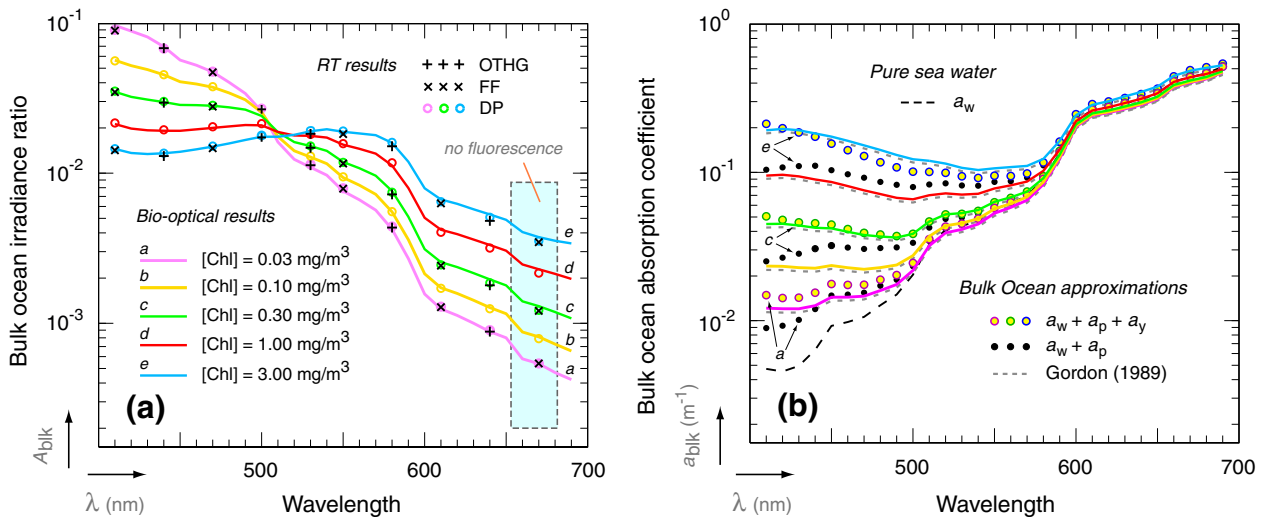


Fig. 3. (a) Ocean body irradiance ratios A_{blik} just below the ocean surface as a function of wavelength λ and Chlorophyll a concentration $[\text{Chl}]$. Curves (a–e): Bio-optical model results from Section 3.2. Plus symbols ('OTHG'): Radiative transfer (RT) results for one-term Henyey–Greenstein bulk ocean scattering functions (see OTHG curves in Fig. 2 for $\lambda = 410$ and 550 nm). Cross symbols ('FF'): RT results for Fournier–Forand bulk ocean scattering functions (see FF curves in Fig. 2 for $\lambda = 410$ and 550 nm). Open circles ('DP'): RT results for detritus-plankton bulk ocean scattering functions (see DP curves in Fig. 2 for $\lambda = 410$ and 550 nm). (b) Bulk ocean absorption coefficients a_{blik} as a function of wavelength λ and Chlorophyll a concentration $[\text{Chl}]$. Solid curves (a–e): a_{blik} retrieved from K_{blik} (used for curves a–e in Fig. 3a). Open circles: $a_{\text{blik}} = a_w + a_p + a_y$ (used for open circle results in Fig. 4a). Solid circles: $a_{\text{blik}} = a_w + a_p$ (used for solid circle results in Fig. 4a). Short-dash curves: a_{blik} retrieved from approximation by Gordon (1989). Shown also (long-dash curve) are the results a_w for pure sea water only.

for the entire range of λ and [Chl]. In Fig. 3a, we also include results from RT computations in which F_p is represented by a Fournier–Forand (FF) scattering function (Fournier & Forand, 1994; Fournier & Jonasz, 1999) and by a one-term Henyey–Greenstein (OTHG) function (Henyey & Greenstein, 1941). The refractive index m for the FF functions is varied according to Mobley et al. (2002), and the asymmetry parameter g_p for the OTHG functions according to Haltrin (2002), to fit the backscattering efficiency q_p in Table 2. The corresponding values for m and g_p are listed in Table 2, and the resulting scattering functions are shown in Fig. 2. We observe in Fig. 3a again excellent agreement between these RT results and the semi-analytical spectra of A_{blk} . The variation in Table 2 of g_p with [Chl] can be reproduced by the following polynomial fit:

$$g_p(\text{Chl}) = 0.95038 + 0.0108(x_{\text{Chl}}) + 0.0002(x_{\text{Chl}})^2 (\pm 7 \times 10^{-5}). \quad (21)$$

Note once more that this fit differs from that presented by us in C2006 because of the spectral changes in q_p discussed in Section 3. We refer to Appendix A for a more detailed discussion on the differences between the numerical results presented in C2006 and in the current work. The solid curves in Fig. 3b provide the spectra of a_{blk} derived from K_{blk} and used for the spectra of A_{blk} in Fig. 3a. Also shown in Fig. 3b is the absorption spectrum a_w for pure sea water (from Pope & Fry, 1997), and the approximations for a_{blk} spectra given by Eq. (15) (from Gordon, 1989) and by Eqs. (22)–(24) (from the sum of contributions to a_{blk} ; see discussion below). Note that all a_{blk} spectra converge towards a_w for $\lambda \geq 600$ nm. Furthermore, good agreement with the A_{blk} -derived spectra is observed for the approximation of a_{blk} by Gordon (1989), while the agreement is moderately good for the total sum of approximated contributions to a_{blk} .

In Fig. 4a and b, we evaluate the changes in the RT values of A_{blk} that are caused by changes in the bio-optical constraints on the scattering properties of bulk oceanic waters. Specifically, instead of using empirical relationships for the attenuation coefficient K_{blk} of bulk oceanic water to obtain a_{blk} as in Section 3.2 we separate a_{blk} into the contributions from various oceanic constituents, quantify each of these contributions separately, and examine the effect on A_{blk} of absorption by CDOM. Furthermore, instead of using variable mixtures

of detritus and plankton particles to produce realistic changes in the backscattering coefficient s_{blk} (see Section 3.3), we consider a compositionally constant sample of ‘typical’ plankton particles. For a_{blk} , we write

$$a_{\text{blk}}(\lambda) = a_w(\lambda) + a_p(\lambda) + a_y(\lambda) \quad (22)$$

where a_w , a_p and a_y are the absorption coefficients for pure sea water, for the total (i.e., living and non-living) suspended particulate, and for yellow substance (i.e., CDOM), respectively. The values for a_w are taken from Pope and Fry (1997) as in Section 3.2, whereas for a_p and a_y we use the empirical relationships provided by Bricaud et al. (1998, 1999) and Morel and Gentili (2009), respectively. The former relationship is based on analyses of 1100+ open ocean samples, and reads as

$$a_p(\lambda) = \alpha(\lambda)[\text{Chl}]^{\beta(\lambda)}. \quad (23)$$

where α and β are regression coefficients obtained from linear regression of log-transformed values of a_p and [Chl] data. The relationship for a_y on the other hand is an indirect estimate based on the difference at $\lambda = 400$ nm between a_{blk} (minus a_w) computed from Section 3.2 and a_p computed from Eq. (23). An exponential decrease is assumed for larger wavelengths where the contribution of a_y to a_{blk} decreases rapidly and therefore becomes difficult to retrieve. The resulting relationship is

$$a_y(\lambda) = 0.065[\text{Chl}]^{0.63} e^{-S(\lambda-400)} \quad (24)$$

where the spectral slope variable S is set to 0.018 nm^{-1} (Morel & Gentili, 2009). We refer to Fig. 3b for a comparison between the resulting $a_{\text{blk}} = a_w + a_p + a_y$ values (open circles) and $a_{\text{blk}} = a_w + a_p$ values (black solid circles), and the a_{blk} values from Section 3.2 (solid and short-dash curves). For the ‘typical’ plankton particles we adopt the findings of Morel (1973) who, assuming a single Junge-type differential size-distribution of spherical particles with exponent γ and a single refractive index m , found that $\gamma = 4$ and $m = 1.05$ provided the best fit to measurements of underwater light scattering functions. Note that this fit does not include polarization measurements (Morel, 1973), the associated size

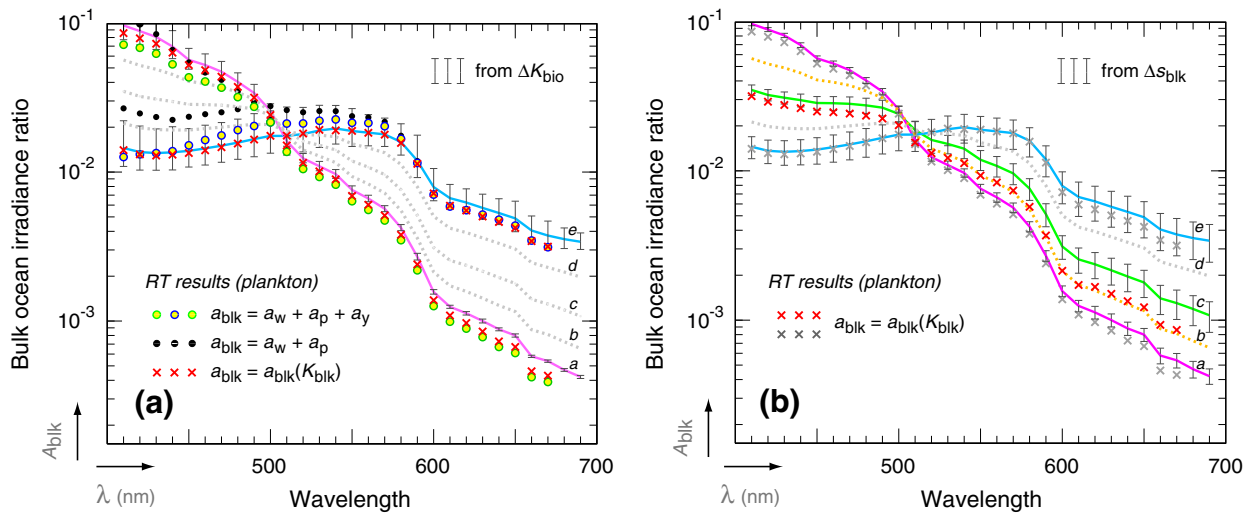


Fig. 4. (a) The ocean body irradiance ratio A_{blk} just below the ocean surface as a function of wavelength λ and Chlorophyll *a* concentration [Chl]. Curves (a–e): same bio-optical results as curves a–e in Fig. 3a. Error bars: Uncertainty in A_{blk} computed from root-mean-square error (RMSE) values for K_{blk} . Solid circles: RT results for plankton bulk ocean scattering functions and $a_{\text{blk}} = a_w + a_p$ (cf. solid circles in Fig. 3b). Open circles: RT results for plankton bulk ocean scattering functions and $a_{\text{blk}} = a_w + a_p + a_y$ (cf. open circles in Fig. 3b). Crosses: RT results for plankton bulk ocean scattering functions and a_{blk} derived from K_{blk} (cf. solid curves in Fig. 3b). (b). Curves (a–e): same bio-optical results as curves a–e in Fig. 3a. Error bars: Uncertainty in A_{blk} computed from RMSE values for s_{blk} . Crosses: RT results for plankton bulk ocean scattering functions and a_{blk} derived from K_{blk} (cf. solid curves in Fig. 3b). (For interpretation of the color references in this figure legend, the reader is referred to the web version of this article.)

distribution and refractive index are considered typical for plankton (Mobley, 1994), and the resulting backscattering efficiency q_p (i.e., 0.0050) is smaller than that for the D–P models if $[\text{Chl}] \leq 3 \text{ mg/m}^3$ (cf. Table 2). The RT values of A_{blk} for these particles are shown in Fig. 4a by the open circles for $a_{\text{blk}} = a_w + a_p + a_y$, by the black solid circles for $a_{\text{blk}} = a_w + a_p$, and by the red crosses for the bio-optical a_{blk} values from Section 3.2 (see Table 2 for $\lambda = 410$ and 550 nm). Note that in this figure we consider only $[\text{Chl}]$ values of 0.03 and 3.0 mg/m^3 and the corresponding semi-analytical values of A_{blk} are shown by the purple and blue curves respectively. The error bars in Fig. 4a show the effect of the uncertainties in K_{bio} (Morel et al., 2007) on A_{blk} (cf. Eqs. (7), (8) and (11)). The uncertainties in A_{blk} in the blue part of the spectrum can be primarily attributed to the natural variability in absorption by CDOM as discussed in more detail by other authors (Morel, 2009; Morel & Gentili, 2009; Morel et al., 2007).

Several observations can be made regarding Fig. 4a. Firstly, the RT values of A_{blk} for $a_{\text{blk}} = a_w + a_p + a_y$ (open circles) at $[\text{Chl}] = 3.0 \text{ mg/m}^3$ fall within the error bars of the corresponding semi-analytical values, while at $[\text{Chl}] = 0.03 \text{ mg/m}^3$ they give a slight underestimate compared with the corresponding semi-analytical values. It should be noted though that Eq. (24) was derived using $[\text{Chl}] \geq 0.07 \text{ mg/m}^3$ (see Fig. 3 in Morel, 2009), and that it actually overestimates a_y for $[\text{Chl}] < 0.07 \text{ mg/m}^3$. This causes a_{blk} in Eq. (22) to be unusually large for $[\text{Chl}] = 0.03 \text{ mg/m}^3$ (cf. open circles in Fig. 3b for curve 'a'), and is consistent with the underestimation of A_{blk} by the RT method seen in Fig. 4a for low $[\text{Chl}]$. Secondly, ignoring absorption by CDOM causes the RT values of A_{blk} (black solid circles) to be biased high in the blue wavelength domain, as expected. Note that this bias falls outside the error bars for large $[\text{Chl}]$ and wavelengths shorter than 500 nm. Thirdly, using 'typical' plankton particles instead of the D–P model does not have a large impact on the RT values of A_{blk} for the a_{blk} values of Section 3.2 (red crosses). This last observation is however only true for the boundary values of $[\text{Chl}]$ considered in Fig. 4a. In one case, $[\text{Chl}] = 3.0 \text{ mg/m}^3$, the bulk ocean scattering matrix \mathbf{F}_{blk} is only weakly affected by detritus particle scattering (see f_{det} values in Table 2) and in the other case, $[\text{Chl}] = 0.03 \text{ mg/m}^3$, the effects of particulate scattering are small (see values of b_p in Table 2). A more complete picture emerges from Fig. 4b, which reproduces the RT values of A_{blk} in Fig. 4a for a_{blk} computed as in Section 3.2 (grey crosses) but now includes the RT values for $[\text{Chl}] = 0.30 \text{ mg/m}^3$ (red crosses, curve 'c'). The error bars in this figure show the effect of uncertainties in the natural variability in particulate backscattering, i.e. in the product of q_p and b_p (from Huot et al., 2008), on A_{blk} . In Fig. 4b, we can see that if the variable D–P mixture is replaced by the 'typical' plankton particles the RT values of A_{blk} are noticeably smaller than the semi-analytical ones at $[\text{Chl}] = 0.30 \text{ mg/m}^3$. This difference becomes larger than the uncertainties caused by natural variability in particulate backscattering for $\lambda \geq 500 \text{ nm}$, which is where the bulk ocean scattering matrix \mathbf{F}_{blk} is least affected by pure sea water scattering. Similar decreases in RT values of A_{blk} are seen for $[\text{Chl}] = 0.1$ and 1.0 mg/m^3 when replacing the D–P mixture by 'typical' plankton particles (results not shown here).

5.2. RSP data analyses

In Figs. 5–8, we apply our hydrosol model to the analysis of the contributions of water-leaving radiance to reflectance measurements over open oceans. The upper and lower rows in these figures show the total reflectance

and the linearly polarized reflectance

$$\rho_{\text{pol}} \equiv \frac{\pi(Q^2 + U^2)^{1/2}}{\mu_0 S_0} \quad (26)$$

respectively. In these definitions of reflectance S_0 is the extraterrestrial solar flux for the current Earth–Sun distance and μ_0 is the cosine of the solar zenith angle θ_0 . The left and right columns in these figures show the reflectance at $\lambda = 410 \text{ nm}$ and 550 nm, respectively. The negative and positive viewing angles θ correspond to the fore and aft viewing angles of the RSP instrument. The yellow error bars depict the mean RSP measurements and their associated uncertainty ε , the latter of which is the combined standard error of the measurement uncertainty κ and the scan-to-scan standard error ξ of measurements (see Table 1). Fig. 9 provides a closer look at these measurement uncertainties for RSP files 45 and 55. The reflectance in Fig. 5 (from RSP file 44) and 6 (from RSP file 45) was observed using the RSP at a low altitude of $z = 65 \pm 3 \text{ m}$, and at relative azimuth angles $\varphi - \varphi_0$ of 1.3° and 38° (for the fore direction), respectively. The solar zenith angle θ_0 was approximately 32° for both these files. The reflectance in Fig. 7 (from RSP file 53) and 8 (from RSP file 55) was observed at a mid altitude of $z = 4.1 \text{ km}$ with a small (optical depth ~ 0.01 at 550 nm) aerosol/cirrus loading above the plane. The relative azimuth angle $\varphi - \varphi_0$ for these files was (for the aft direction) 3.8° and 56.5° , respectively, and the solar zenith angle θ_0 was approximately 40° . The flight tracks for RSP files 44, 45, and 53 were closer to each other ($< 40 \text{ km}$) than to RSP file 55, which was acquired about 75 km away (see Fig. 1). The numbers of scans that are averaged together in Figs. 5–8 are much larger for the low-altitude flights (i.e. > 100 for RSP files 44 and 45) than for the mid-altitude flights (i.e. < 5 for RSP files 53 and 55) to compensate for the noise caused by the glitter of skylight reflected off the small ($< 1 \text{ m}^2$) sample of ocean surface slopes within each field of view. The flight track segments selected cover much of RSP files 44 and 45, while for RSP files 53 and 55 they cover sections that have the smallest estimated aircraft roll and pitch angles.

The black dashed curves in these figures show the results of RT computations if we ignore contributions of water leaving radiance. The aerosol single-scattering properties were retrieved by analyzing the full spectrum of polarized and unpolarized reflectance measured by the RSP at mid altitudes and at azimuth angles close to the solar principal plane, where even in the visible part of the spectrum the contribution of polarized water-leaving radiance is relatively small, as explained in C2006 (see also Fig. 7). The retrieval from these reflectance and polarized reflectance observations of nonspherical salt-like aerosols was based on extensive sensitivity analyses of light scattered by particles with varying refractive indices, sizes, and aspect ratio distributions using the statistical approach to light scattering developed in (Mishchenko et al., 1997) and the spheroid scattering data base documented in (Dubovik et al., 2006). A discussion of these analyses is beyond the scope of this study which is focused on how well the polarized radiance emerging from case 1 waters can be computed using our D–P mixture. However, we do note that the use of observations at 865, 1590 and 2250 nm ensures that our aerosol single-scattering properties are an acceptable representation of the true column scattering properties, independent of the ocean color contribution to the observed reflectance. We summarize in Table 4 the single scattering properties of fine and coarse mode aerosols used for Figs. 5–8. For the reflectance in Figs. 5 and 6, we assumed most of the aerosol to reside above the aircraft (except for a thin haze of water droplets) and varied the optical thicknesses of the aerosol modes to fit the upward looking AATS-14 data that was acquired simultaneously. For the reflectance in Figs. 7 and 8, we assumed all aerosols to reside below the aircraft and varied the optical thicknesses of the two aerosols modes to give a best fit to all of the RSP data. The values of these thicknesses for the coarse mode aerosol

$$\rho_{\text{tot}} \equiv \frac{\pi I}{\mu_0 S_0} \quad (25)$$

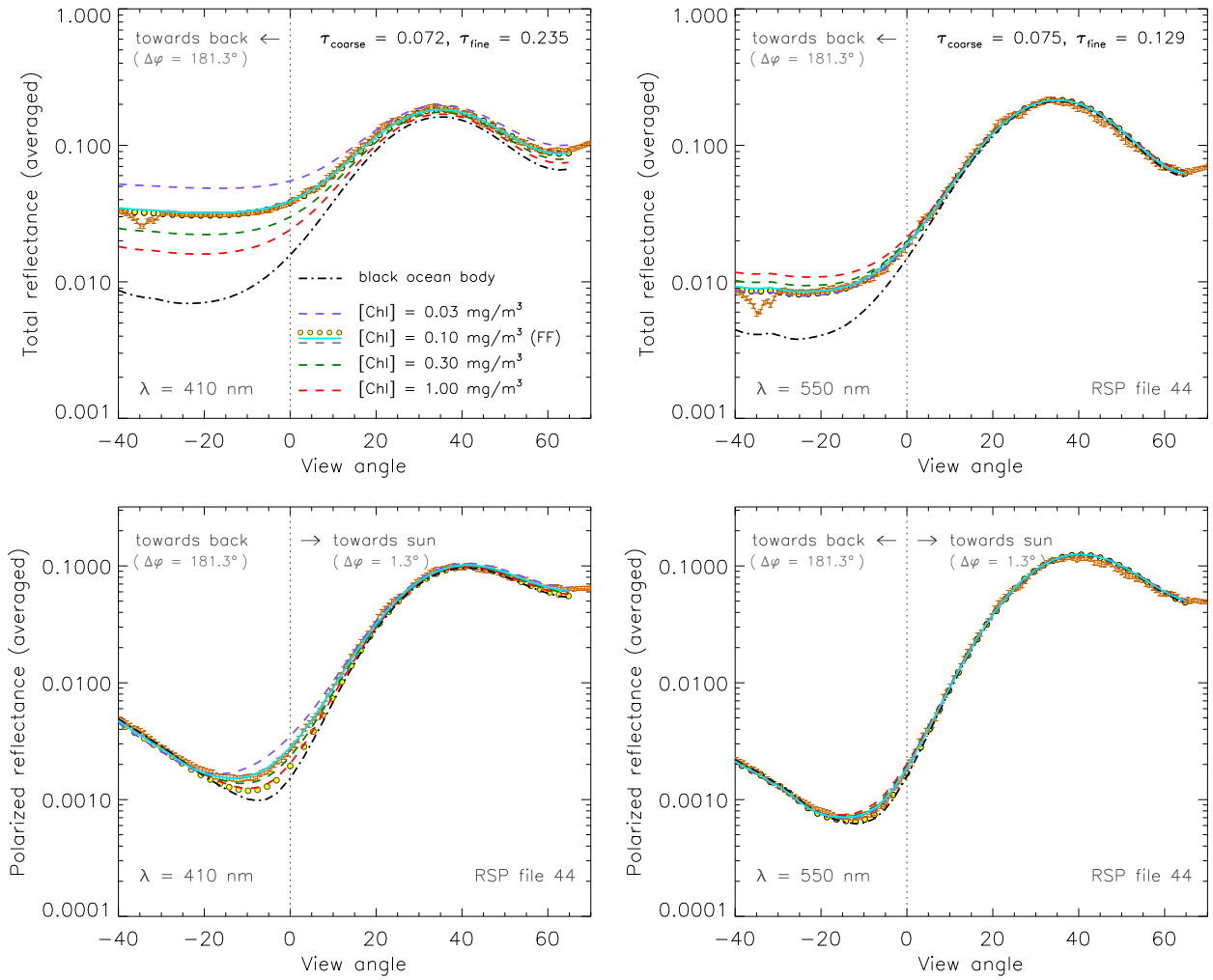


Fig. 5. Analyses of RSP file 44 data obtained at an aircraft altitude z of 62 m, and at a relative azimuth angle $\Delta\varphi \equiv \varphi - \varphi_0$ of 1.3° for positive viewing angle θ . Upper and lower panels are for total reflectance ρ_{tot} and polarized reflectance ρ_{pol} , respectively, at $\lambda = 410$ nm (left column) and 550 nm (right column). Yellow lines denote the mean of RSP data, and yellow error bars their standard error ε , as a function of θ . The legend for the corresponding RT results is given in the upper left panel.

(τ_{coarse}) and the fine mode aerosol (τ_{fine}) are given in the upper right corner of the total reflectance panels. The AATS fit for the sum of τ_{coarse} and τ_{fine} in Figs. 5 and 6 is shown in Fig. 10. The sum of these optical thicknesses, and of those given in Figs. 7 and 8, is smaller than the total aerosol optical thickness derived from MODIS/Aqua; however, the differences are in good agreement with the validation results for the MODIS/Aqua aerosol optical thickness by Redemann et al. (2009). Finally, we remark that the bulk aerosol single scattering albedos computed from Table 4 and from τ_{coarse} and τ_{fine} in Figs. 5–8 agree well (within 0.02) with the aerosol scattering albedos retrieved by Bergstrom et al. (2010) from SSFR instrument onboard the J-31 aircraft.

In Figs. 5–8 we show the results of RT computations that include the contribution of radiance emerging from an ideal case 1 ocean containing D–P mixtures with [Chl] of 1.0, 0.30 and 0.03 mg/m^3 (dashed red, green, grey, and purple curves respectively). The solid cyan curves (denoted by ‘ $+\Delta a_{\text{blk}}$ ’ except in Fig. 5) are the RT match to the observations obtained by perturbing the a_{blk} values for [Chl] = 0.10 mg/m^3 from the amounts given in Table 2 to the amounts given in Table 5. From Fig. 5, we observe that the total and polarized reflectance computed for low-altitude observations at $\lambda = 410$ nm shows notable sensitivity to [Chl]. The absolute changes in polarized reflectance are not as large as for total reflectance ($\geq 2.5 \times 10^{-2}$), i.e., they increase from about 1.5×10^{-3} to 8×10^{-3} for increasing positive viewing angles as [Chl] is reduced from 1.0 mg/m^3 to 0.03 mg/m^3 . The significance of these variations in

polarized reflectance with [Chl] are more apparent in the *relative* change in polarized reflectance (referenced hereafter to the case for [Chl] = 0.03 mg/m^3), which varies from about 6% in the sunglint to more than 40% in the nadir viewing direction. A good match occurs for both the magnitude and bidirectionality of the reflectance at 410 nm for [Chl] = 0.10 mg/m^3 . Note that the match occurs without the need to perturb a_{blk} , i.e., the cyan and grey curves coincide with one another. The polarized reflectance for the nadir-viewing direction (which for principal plane observations is the closest view to a nearby neutral point – see Fig. 14) is quite sensitive to the [Chl], and so the match between the model and the RSP observations for both the reflectance and the polarized reflectance, provides validation of the scattering matrix generated by the D–P hydrosol model at 410 nm. At $\lambda = 550$ nm, we observe that the polarized reflectance is still sensitive to the *presence* of water leaving radiance in the vicinity of the nadir-viewing direction, but the variation of this reflectance with [Chl] is small compared to the standard error ε in RSP measurements. The absolute change with [Chl] is 1.6×10^{-3} for viewing angles close to $+60^\circ$ and much less for smaller positive viewing angles, which causes the relative change to be less than 1% in the sun glint and about 10% near the nadir-viewing direction for $[\text{Chl}] \leq 1.0 \text{ mg}/\text{m}^3$ (although the relative change is much less than 10% for $[\text{Chl}] \leq 0.3 \text{ mg}/\text{m}^3$). The total reflectance retains its sensitivity to variations in [Chl] and a match is obtained to the RSP observations with the same value of [Chl] = 0.1 mg/m^3 that matched the observations at 410 nm. This

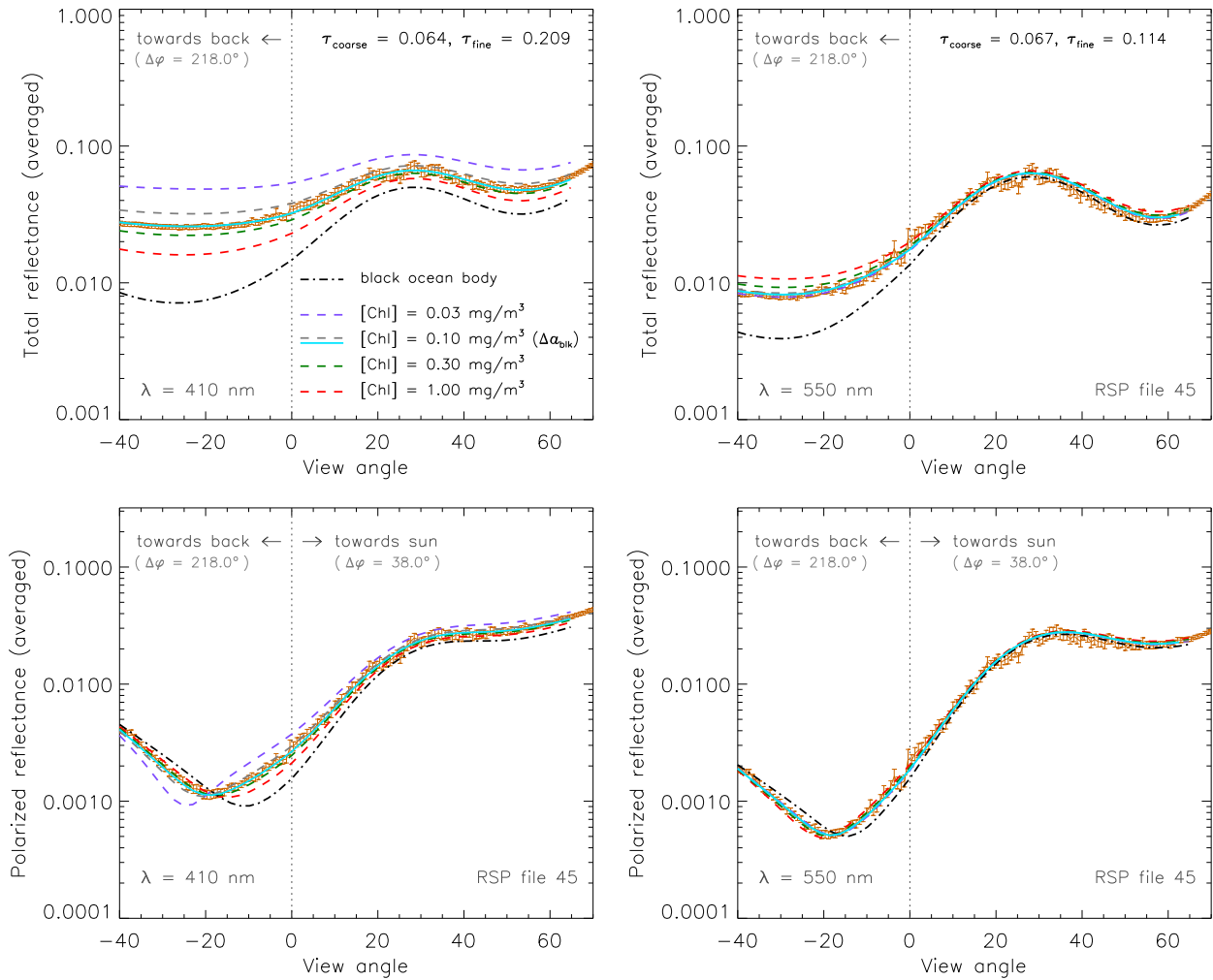


Fig. 6. Analyses of RSP file 45 data obtained at an aircraft altitude z of 68 m, and at a relative azimuth angle $\Delta\varphi \equiv \varphi - \varphi_0$ of 38° for positive viewing angle θ . Upper and lower panels are for total reflectance ρ_{tot} and polarized reflectance ρ_{pol} , respectively, at $\lambda = 410$ nm (left column) and 550 nm (right column). Yellow lines denote the mean of RSP data, and yellow error bars their standard error ε , as a function of θ . The legend for the corresponding RT results is given in the upper left panel.

demonstrates the coherence of the spectral variations in the D–P model for wavelengths that are in very different ocean body scattering regimes.

For comparison, we included in Fig. 5 the results of RT computations (see open circles) for $[\text{Chl}] = 0.1 \text{ mg/m}^3$ using Fournier–Forand (‘FF’) bulk ocean scattering functions. As expected from the agreement between the FF and D–P bulk ocean scattering functions (cf. Fig. 2), we observe a reasonably good match for the total reflectance measurements. There is some underestimation because the FF bulk ocean scattering functions lack the glory feature (i.e., increased scattering at $\theta = 180^\circ$) of the D–P bulk ocean scattering functions. But Fig. 5 shows that the resulting difference in total reflectance is small at 410 nm (i.e., 4% for negative viewing angles) compared to the computed change with $[\text{Chl}]$, while at 550 nm it is comparable (i.e., 3.5% for negative viewing angles) to the standard error of RSP total reflectance measurements. The RT results for the polarized reflectance are, on the other hand, significantly lower than the RSP measurements especially at 410 nm. That is because the FF functions, and the one-term Henyey–Greenstein functions as well (RT results not shown in Fig. 5), do not prescribe the polarization of scattered light. This produces particulate scattering matrices \mathbf{F}_p whose elements apart from the (1,1) element are set to zero, and leads in underwater light radiative transfer computations to the *depolarization* of light scattered by pure sea water. We remark that Zhai et al. (2010) address this problem by multiplying the FF functions with so-called reduced Mueller matrices

for underwater light polarization to obtain artificial but viable \mathbf{F}_p matrices for vector radiative transfer computations. A comparison of RT results for polarized water-leaving radiance computed with such scattering matrices remains the topic for a future paper.

In Fig. 6, which shows observations and RT calculations for a meridional plane 38° from the solar principal plane, the predicted sensitivity of polarized reflectance at 410 nm to $[\text{Chl}]$ is larger than that seen in Fig. 5 for which the viewing geometry was very close to the solar principal plane. This can be attributed to the decrease in masking by sunglint, and to the viewing geometry crossing a neutral point (see Fig. 14 and subsequent discussion). For example, the absolute change with $[\text{Chl}]$ of the polarized reflectance is similar to that shown in Fig. 5 for positive viewing angles, but the corresponding relative changes are now a factor of 2–3 larger towards the scan edge (e.g., 18% in the sunglint region) and exceed everywhere the RSP measurement uncertainties ε except at $\theta \approx -20^\circ$ (see also upper row in Fig. 9). The relative changes become even higher in the vicinity of the neutral point, i.e. they exceed 80% at $\theta \approx -27^\circ$. We again find the expected large sensitivity of total reflectance at 410 nm to variations in $[\text{Chl}]$ and obtain a good match (cyan curves) for all view angles if $[\text{Chl}] = 0.10 \text{ mg/m}^3$, but with a_{blk} elevated by 30%. The calculated dependence of polarized reflectance at 550 nm on $[\text{Chl}]$ is similar to that shown in Fig. 5 with the absolute change being much smaller than at 410 nm and everywhere within the measurement

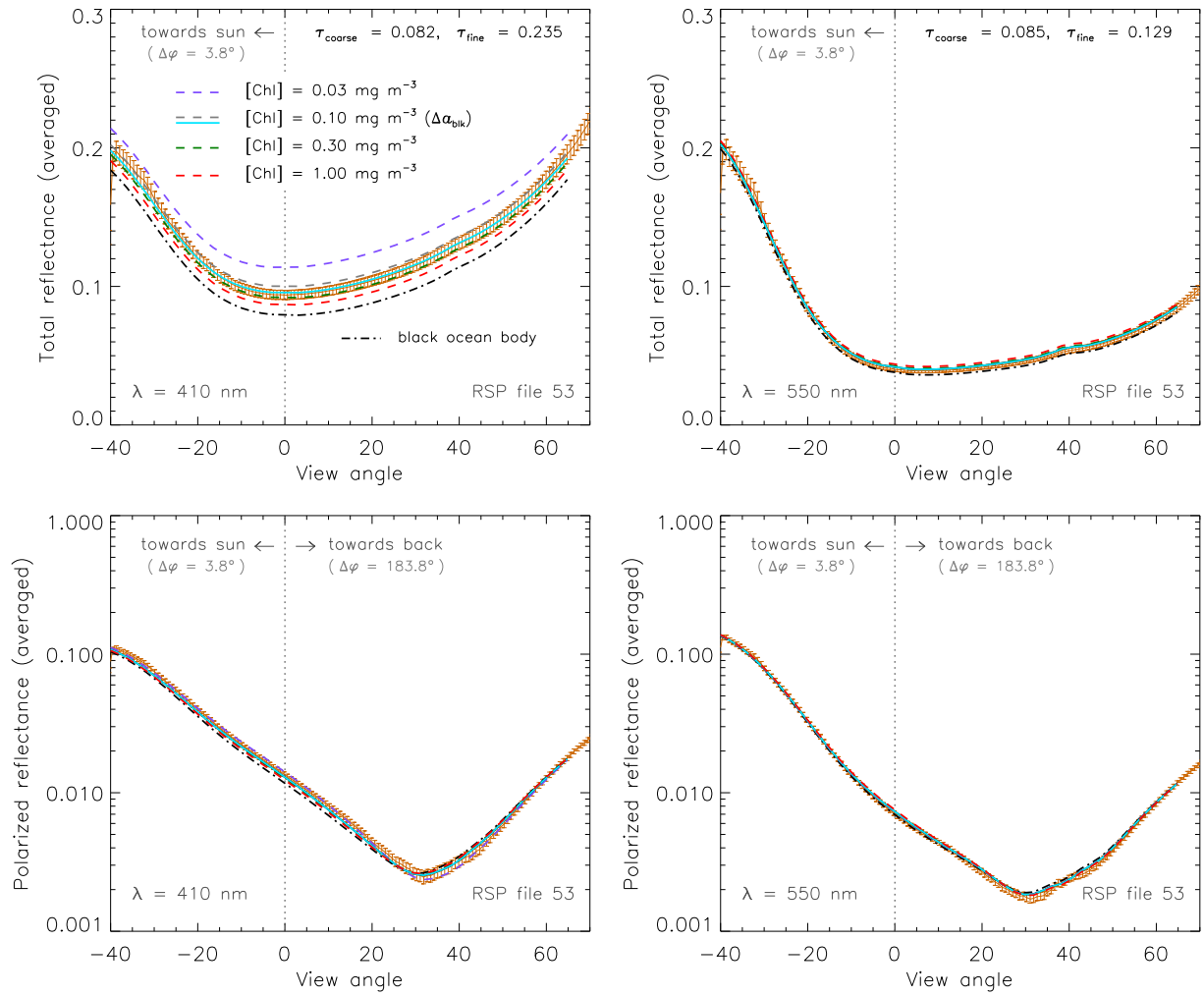


Fig. 7. Analyses of RSP file 53 data obtained at an aircraft altitude z of 4.1 km, and at a relative azimuth angle $\Delta\varphi \equiv \varphi - \varphi_0$ of 3.8° for negative viewing angle θ . Upper and lower panels are for total reflectance ρ_{tot} and polarized reflectance ρ_{pol} , respectively, at $\lambda = 410$ nm (left column) and 550 nm (right column). Yellow lines denote the mean of RSP data, and yellow error bars their standard error ε , as a function of θ . The legend for the corresponding RT results is given in the upper left panel.

uncertainties ε for $[\text{Chl}] \leq 0.3 \text{ mg/m}^3$. The total reflectance observed at 550 nm is matched within the RSP measurement uncertainties for same $[\text{Chl}]$ of 0.1 mg/m^3 as required to match the 410 nm observations with only a slight (5%) perturbation to a_{blk} . The large value of a_{blk} required to fit the blue observations suggests elevated amounts of CDOM for this track (see also discussion in Section 5.3) which is quite possible given the proximity to land. We remark that reducing a_{blk} in the blue and increasing $[\text{Chl}]$ to 0.30 mg/m^3 also provides a viable match to the RSP reflectance at 410 nm (result not shown here) but Fig. 6 shows that such a high $[\text{Chl}]$ does not match the 550 nm observations.

In Fig. 7, we see that, for mid-altitude observations close to the solar principal plane, the sensitivity of polarized reflectance at 410 nm to $[\text{Chl}]$ predicted by RT calculations is considerably reduced compared to the low-altitude observations (cf. Fig. 5) as a result of the intervening atmosphere. The absolute change in polarized reflectance approaches 2×10^{-3} for the nadir-viewing direction but the corresponding relative change is now less than 13% (the changes towards the scan edge in the sunglint region are $\geq 5 \times 10^{-3}$ and $\leq 5\%$, respectively). The largest relative changes in polarized reflectance now occur in the vicinity of a polarization minimum near the back-scattering direction, but do not exceed 16% and the standard error ε for RSP reflectance is also substantial around this minimum. All changes for polarized reflectance at 550 nm seen in Fig. 7 are a factor

of four or more less than at 410 nm. This leads to a maximum relative change in polarized reflectance at 550 nm of less than 4% near the nadir-viewing direction (the absolute and relative changes in the sunglint region are $\leq 1.5 \times 10^{-3}$ and $\leq 1\%$, respectively). As expected the total reflectance at mid altitude, as shown in Fig. 7, is far less sensitive to changes in $[\text{Chl}]$ than low-altitude observations. The only constraint imposed on $[\text{Chl}]$ by mid-altitude measurements at 550 nm is that $[\text{Chl}] \leq 0.3 \text{ mg/m}^3$. At 410 nm it is clear that the best match to the observations is obtained with $[\text{Chl}] = 0.10 \text{ mg/m}^3$ where the elevated amount of a_{blk} is the same as that required to match the RSP total reflectance for the low-altitude observations of File 45.

Finally, in Fig. 8 we observe that even for mid-altitude observations the polarized reflectance at 410 nm has sensitivity to variations in $[\text{Chl}]$ as one moves away from the solar principal plane. Even though the absolute changes with $[\text{Chl}]$ in this reflectance are similar to those in Fig. 7 in the azimuth half-plane closest to sunglint, the corresponding relative change in polarized reflectance increases by a factor of up to 2 towards large viewing angles (i.e., it approaches 11% in the sunglint region). The polarization minimum in Fig. 8 does not coincide with a neutral point (although it is close to one – see Fig. 15). Hence we do not observe the large variations with $[\text{Chl}]$ that were found near the neutral point in Fig. 6. Nevertheless, the relative change in polarized reflectance approaches 18% in this minimum,

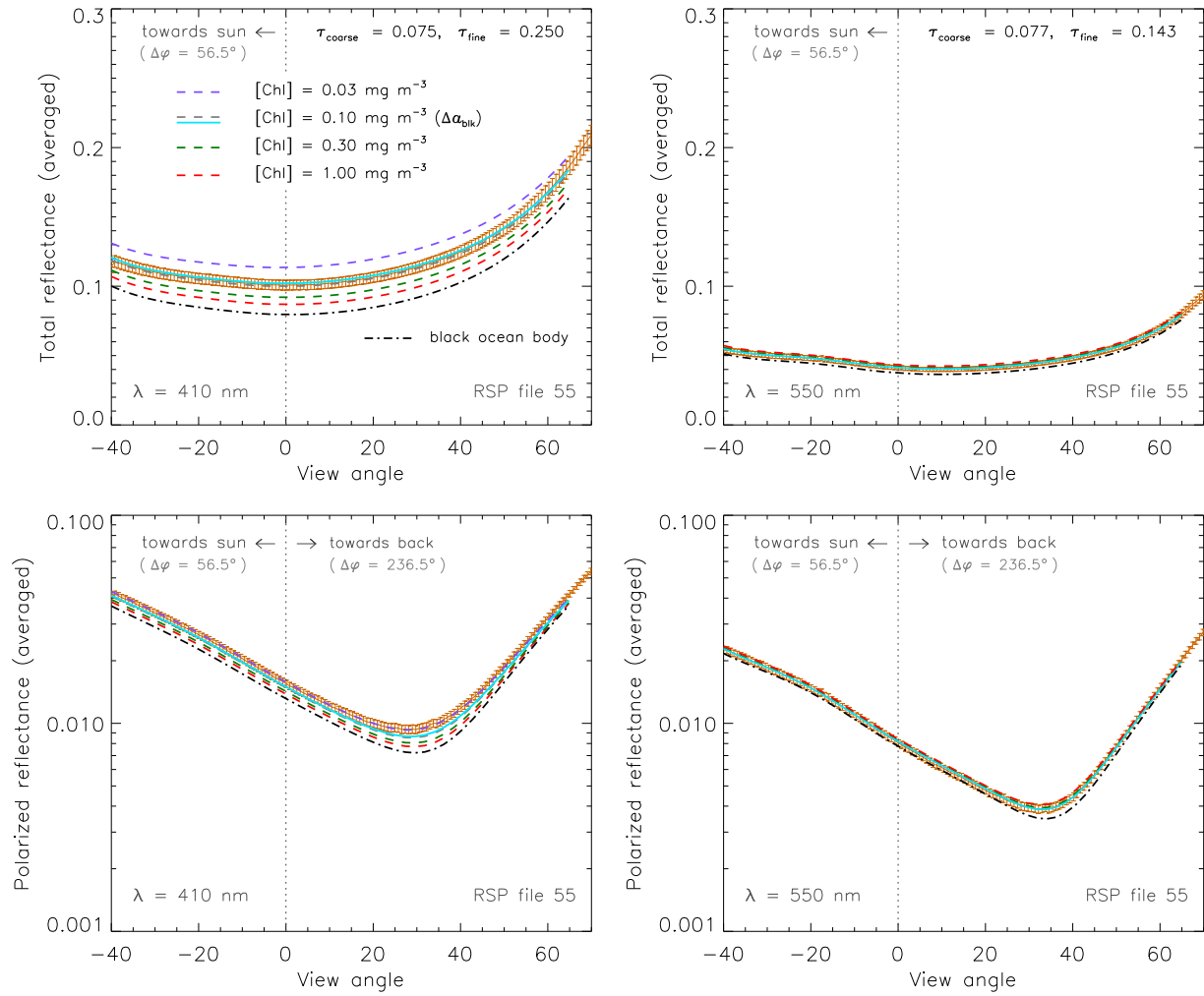


Fig. 8. Analyses of RSP file 55 data obtained at an aircraft altitude z of 4.1 km, and at a relative azimuth angle $\Delta\varphi \equiv \varphi - \varphi_0$ of 56.6° for negative viewing angle θ . Upper and lower panels are for total reflectance ρ_{tot} and polarized reflectance ρ_{pol} , respectively, at $\lambda = 410$ nm (left column) and 550 nm (right column). Yellow lines denote the mean of RSP data, and yellow error bars their standard error ε , as a function of θ . The legend for the corresponding RT results is given in the upper left panel.

and it remains everywhere larger than the standard error ε in RSP reflectance (see also lower row in Fig. 9). At 550 nm, we observe a small-to-negligible sensitivity of the RSP total reflectance and polarized reflectance to variations in $[\text{Chl}]$ with any $[\text{Chl}] \leq 0.3$ mg/m^3 providing an acceptable match to the observations. The total reflectance at 410 nm retains its sensitivity to variations in $[\text{Chl}]$, and a match is obtained to the RSP measurements with $[\text{Chl}] = 0.10$ mg/m^3 and slightly smaller values for a_{blk} than required for files 45 and 53. Note that the corresponding match for the polarized reflectance is not as good, i.e. it occurs at the fringes of the RSP error bars. We find that the poor quality of this fit is the result of a small roll ($\sim 1^\circ$) of the aircraft – see Figs. 14–15 and related discussion on sunglint profiles. It can be seen from these figures that the effects of uncertainties in viewing geometry will have the largest effect in the vicinity of polarization minima and increase with decreasing wavelength.

Fig. 9 summarizes the changes in polarized reflectance with $[\text{Chl}]$, and examines the angular variation of this change, for viewing geometries outside the sunglint. The upper and lower panels in this figure relate to the polarized reflectance of RSP files 45 and 55, and the left and right columns are for $\lambda = 410$ nm and 550 nm, respectively. The yellow error bars show the standard error ε for RSP reflectance, i.e. they are the same yellow error bars as in Figs. 6 and 8 except for subtracting the mean RSP reflectance for each viewing angle. The grey and cyan error bars in Fig. 9 show the contributions to ε of the

measurement uncertainty κ (computed for a calibration uncertainty ζ of 3.5% and an uncertainty η for the degree of linear polarization of 0.2%) and of the scan-to-scan standard error ξ , respectively. Note that ξ is large for RSP file 45 if $\theta > 0^\circ$ because of the relatively close proximity to the sunglint (see also Fig. 14). For other viewing geometries, it remains smaller for RSP file 45 than for RSP file 55 because of the larger number of scans averaged together in the analysis of the former file. The blue, green, and red dashed lines in Fig. 9 show the changes (i.e., differences) in polarized reflectance that are computed for the viewing geometry and aircraft altitude representative of these files if $[\text{Chl}]$ increases from a base value of 0.03 mg/m^3 to 0.1 mg/m^3 , 0.3 mg/m^3 , or 1.0 mg/m^3 , respectively. Note that the changes in the first column are negative because reflectance decreases at 410 nm with increasing $[\text{Chl}]$ (cf. Fig. 3a). Comparing the changes in polarized reflectance with the measurement uncertainties ε affirms the conclusions drawn from Figs. 5–8. That is, for off-glint observations at 410 nm, perturbations of $[\text{Chl}]$ from oligotrophic values found in the central gyres of oceans (0.03 mg/m^3) cannot be ignored regardless of the observational altitude. At 550 nm it is only when $[\text{Chl}] > 0.3$ mg/m^3 that a difference from oligotrophic conditions is apparent. Another feature of Fig. 9 is that the angular variations in polarized reflectance caused by $[\text{Chl}]$ are the same for different perturbations in $[\text{Chl}]$. This is illustrated by the fact that scaling the perturbation from 0.03 mg/m^3 to 0.1 mg/m^3 by a spectrally

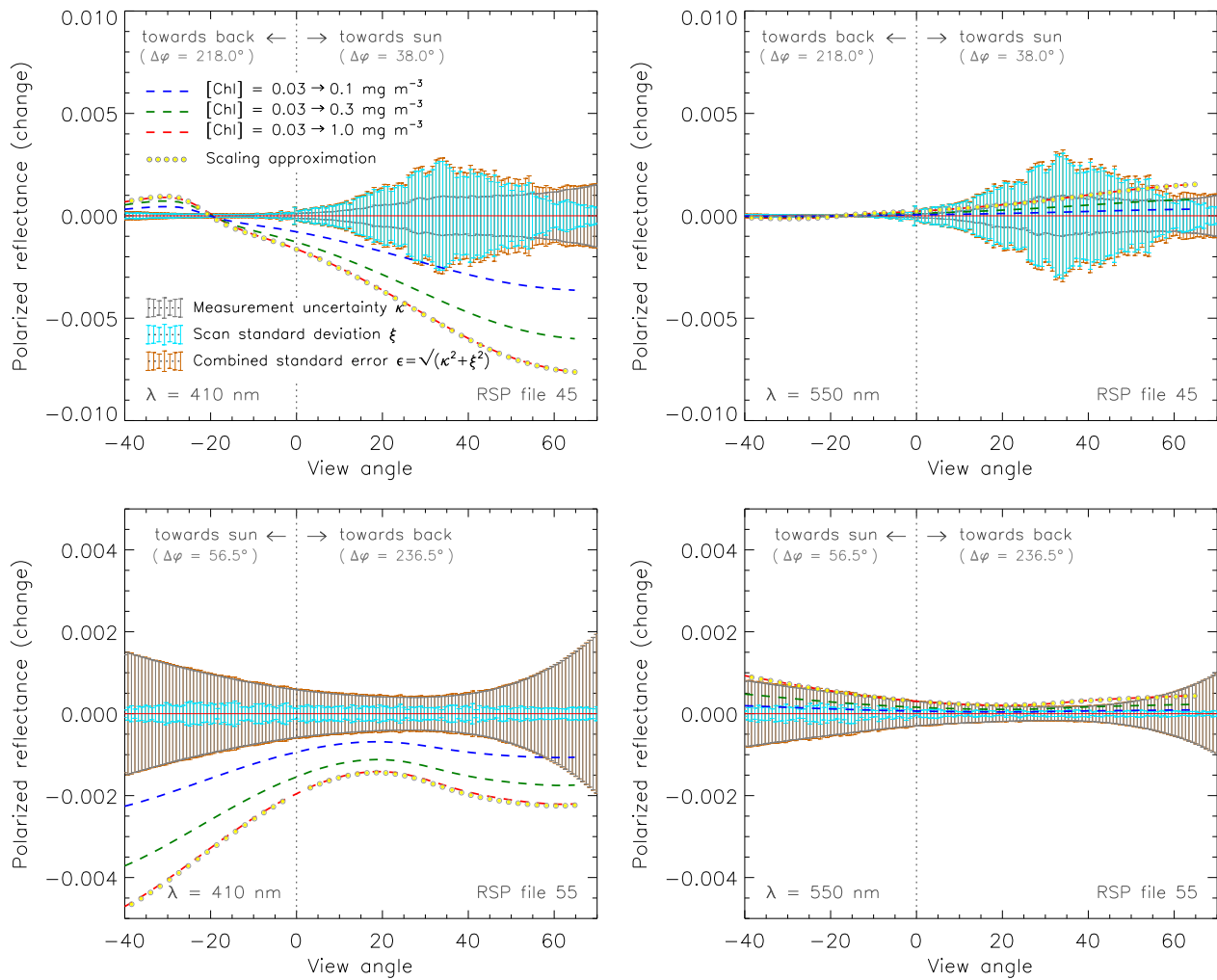


Fig. 9. Isolated uncertainties in RSP polarized reflectance (error bars), and isolated changes in RT polarized reflectance with [Chl] (dashed lines), as a function of viewing angle θ . Upper and lower panels are for RSP files 45 and 55, respectively, at $\lambda = 410$ nm (left column) and 550 nm (right column). The legend for the RSP and RT results is given in the upper left panel.

dependent factor (2.1 at 410 nm and 4.7 at 550 nm shown as yellow circles) provides an excellent match to the perturbation from 0.03 mg/m³ to 1.0 mg/m³ (red dashed line). Hence, while the polarized radiance emerging from open oceans containing D–P like matter can change substantially with viewing angle for a given [Chl] and with [Chl] for a given viewing angle, the angular shape of the polarized reflectance does not vary noticeably with [Chl].

In Table 5 we compare our retrieved values of [Chl] with those retrieved from MODIS/Aqua data for the same locations and dates. In addition, we provide the corresponding MODIS/Aqua retrievals at $\lambda = 490$ nm of the diffuse attenuation coefficient K_{blk} , and the

computed (i.e. bio-optical) values of a_{blk} and K_{blk} for the MODIS/Aqua [Chl] values. The comparisons for the RSP and MODIS/Aqua [Chl] values are satisfactory given the fact that we did not consider [Chl] values between 0.10 and 0.30 mg/m³ in our RT computations and MODIS nominal uncertainties in [Chl] retrieval are about 30% (Esaías et al., 1998; Moore et al., 2009). Comparisons with Table 2 show that our a_{blk} values differ by up to 30% at $\lambda = 410$ nm, and up to 5% at $\lambda = 550$ nm, compared to those computed for an ideal case 1 ocean with [Chl] = 0.10 mg/m³. Had we varied [Chl] in smaller increments then, judging from Figs. 6 and 7 we would probably have retrieved slightly larger [Chl] values than 0.10 mg/m³ for RSP Files 45 and 53, respectively. Note that this would also have decreased the perturbations to a_{blk} at 410 nm that we imposed. Indeed, Table 5 shows that the bio-optical values of a_{blk} computed for the MODIS/Aqua retrievals of [Chl] are only slightly smaller than those retrieved from RSP Files 45 and 53. Note further in Table 5 that the K_{blk} values at $\lambda = 490$ nm retrieved from MODIS/Aqua data for various [Chl] are very close to the corresponding bio-optical values of K_{blk} values. The perturbations in a_{blk} at $\lambda = 410$ nm are then consistent with a case 1 ocean that is standard except for some variation in CDOM (Fig. 4a shows that the impact of CDOM on the brightness of a case 1 ocean is significantly reduced at $\lambda = 490$ nm if [Chl] is small). This justifies the use in this work of a D–P hydrosol mixture, which was specifically

Table 4
Aerosol properties of fine and coarse mode particles retrieved from RSP file 53.

Aerosol mode	Effective radius ^a	Effective variance ^b	Shape	Refractive index ^c
Fine	0.15	0.1	Spherical	$1.45 - 0.01i$
Coarse	2.0	1.0	Spheroidal ^d	$1.45 - 0.0005i$

^a ± 0.025 for fine mode and ± 0.5 for coarse mode, in μm .

^b ± 0.05 for fine mode and ± 0.5 for coarse mode.

^c ± 0.01 for real part and ± 0.005 for imaginary part, $\lambda \leq 670$ nm.

^d Equi-probable aspect ratio distribution.

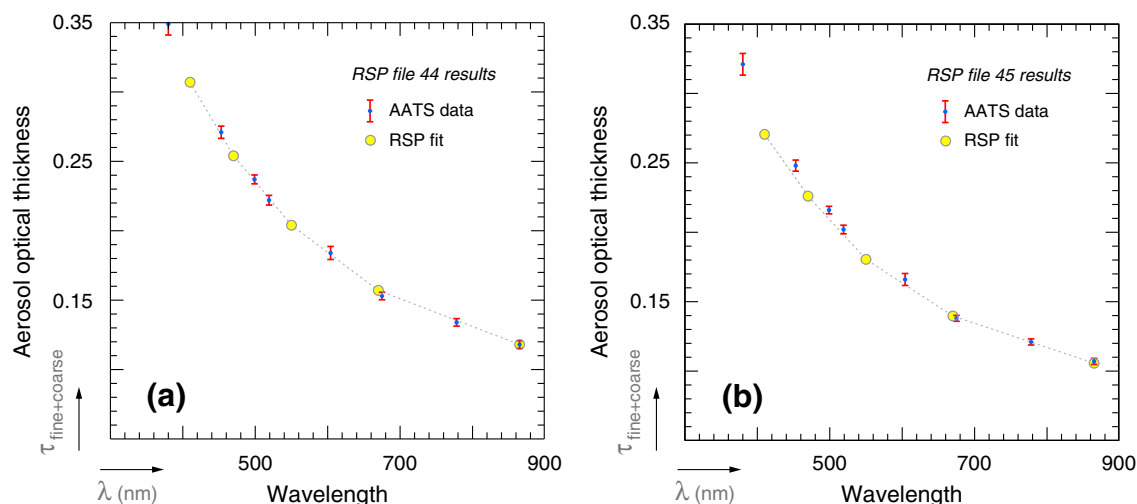


Fig. 10. (a). Optical depth of aerosol above the aircraft for RSP file 44. Blue dots: AATS measurements. Red error bars: standard error of the AATS measurements. Open circles: fit for the AATS measurements assuming the same aerosol microphysical properties as retrieved from RSP file 53 at mid-altitude (Table 4). (b). Same as Fig. 10a but for the optical depth of aerosol above the aircraft for RSP file 45. (For interpretation of the color references in this figure legend, the reader is referred to the web version of this article).

developed for multiple-scattering computations of polarized light in such oceans.

5.3. Discussions and applications

5.3.1. CDOM variations

Our analyses of RSP data show that perturbations in the bulk ocean absorption coefficient a_{blk} affect the total reflectance substantially (e.g., the grey and cyan curves in Fig. 6 differ by up to >30%) but not the polarized reflectance. This implies that the polarized reflectance will be less sensitive to uncertainties in absorption by CDOM than the total reflectance. Note further that the magnitude of this absorption (see Fig. 3b) and its impact on A_{blk} (see Fig. 4a) is significantly reduced at 550 nm compared to 410 nm. In fact, the remotely sensed polarized reflectance computed at 550 nm shows virtually no sensitivity to variations in water-leaving radiance for $[\text{Chl}] \leq 0.3 \text{ mg/m}^3$ (see Figs. 5 and 6). Therefore variations with CDOM of polarized water-leaving radiance at 550 nm can be ignored all together for most of the open ocean. To investigate the impact on water-leaving radiance of anomalies in CDOM absorption at shorter wavelengths, we re-examine in Fig. 11 the total and polarized reflectance observed by the RSP at low altitudes for a wavelength of 410 nm. The yellow lines and error bars in left and right columns of this figure show the same reflectance measurements and associated uncertainties ε as the ones in the left columns of Figs. 5 and 6 (i.e., for RSP files 44 and 45), respectively. The grey and red dashed curves show the corresponding RT results for $[\text{Chl}] = 0.1$ and 1.0 mg/m^3 , respectively, and the cyan curve is the RT best fit to the observed

reflectance using a perturbed value of a_{blk} . The cyan and red error bars show RT calculated changes in reflectance for $[\text{Chl}] = 0.1$ and 1.0 mg/m^3 , respectively, if a_{blk} in Eq. (7) is perturbed by an amount derived from the root-mean-square error for K_{bio} in Eq. (8). That is, the error bars are representative of uncertainties in reflectance for a given $[\text{Chl}]$ that are caused by uncertainties in CDOM absorption (see discussion in Section 5.1). For comparison, we also included the results for the minimum (no water-leaving radiance; black curves) and maximum (for an ocean with $[\text{Chl}] = 0.03 \text{ mg/m}^3$; purple curves) reflectance generated by our RT computations. There are two features of this figure that stand out. Firstly, the changes in *total* reflectance caused by the natural variability in CDOM absorption at 410 nm are much larger than the measurement uncertainties of the reflectance. Note that we need just such a change for $[\text{Chl}] = 0.1 \text{ mg/m}^3$ to fit the total reflectance of RSP file 45 (right column of Fig. 11). Secondly, the changes in *polarized* reflectance caused by the natural variability in CDOM absorption at 410 nm are comparable to or less than the uncertainty in the observations for $[\text{Chl}] \leq 1.0 \text{ mg/m}^3$. Indeed, the RT results for unperturbed a_{blk} (see grey curve) and perturbed a_{blk} (see cyan curve) both fit the polarized reflectance in RSP file 45. Similar arguments can be made for sensitivity of polarized reflectance to variations in s_{blk} caused by a change in the scattering matrix of marine particulates. That is, substituting D–P matter with a compositionally constant mixture of ‘typical’ plankton particles causes relatively little variation in the bulk ocean irradiance ratio A_{blk} for $\lambda < 500 \text{ nm}$ (see Fig. 4). While variations in A_{blk} become larger at longer wavelengths, they are not likely to affect remotely sensed polarized reflectance that is less sensitive to changes in the bulk ocean properties for this wavelength regime than the total reflectance (e.g., see right column of Fig. 9). Fig. 12 examines in more detail changes in the polarized reflectance caused by CDOM and s_{blk} . The error bars in this figure show the standard error ε , measurement uncertainty κ , and scan-to-scan standard error ξ , for the 410 nm polarized reflectance (yellow, grey, and cyan error bars respectively) of RSP files 44 and 45 (upper row) and of RSP files 53 and 55 (lower row). The RSP uncertainties are compared with the RT calculated difference in polarized reflectance at $[\text{Chl}] = 0.1 \text{ mg/m}^3$ and 1.0 mg/m^3 (blue and red dashed lines respectively) caused by perturbing a_{blk} by the same amount as for Fig. 11. Positive and negative reflectance differences correspond to CDOM-induced negative and positive anomalies in a_{blk} , respectively, and remain comparable to or less than ε for all 4 RSP files. The RT calculated difference in polarized reflectance for $[\text{Chl}] = 0.3 \text{ mg/m}^3$, if the ocean contains a fixed mixture

Table 5

Comparison of RSP-derived and MODIS/Aqua-derived $[\text{Chl}]$ and absorption values with those computed for an ideal case 1 ocean.

RSP track	RSP			MODIS/Aqua		Bio-optical model (case 1 ocean)		
	$[\text{Chl}]^a$	$a_{\text{blk}}(410)^b$	$a_{\text{blk}}(550)^b$	$[\text{Chl}]^a$	$K_{\text{blk}}(490)^b$	$[\text{Chl}]^a$	$a_{\text{blk}}(410)^b$	$K_{\text{blk}}(490)^b$
44	0.1	0.0233	0.0567	0.114	0.0331	0.114	0.0252	0.0328
45	0.1	0.0303	0.0595	0.148	0.0361	0.148	0.0293	0.0360
53	0.1	0.0303	0.0567	0.150	0.0353	0.150	0.0296	0.0362
55	0.1	0.0210	0.0567	0.118	0.0322	0.118	0.0257	0.0332

^a In mg/m^3 .

^b In m^{-1} .

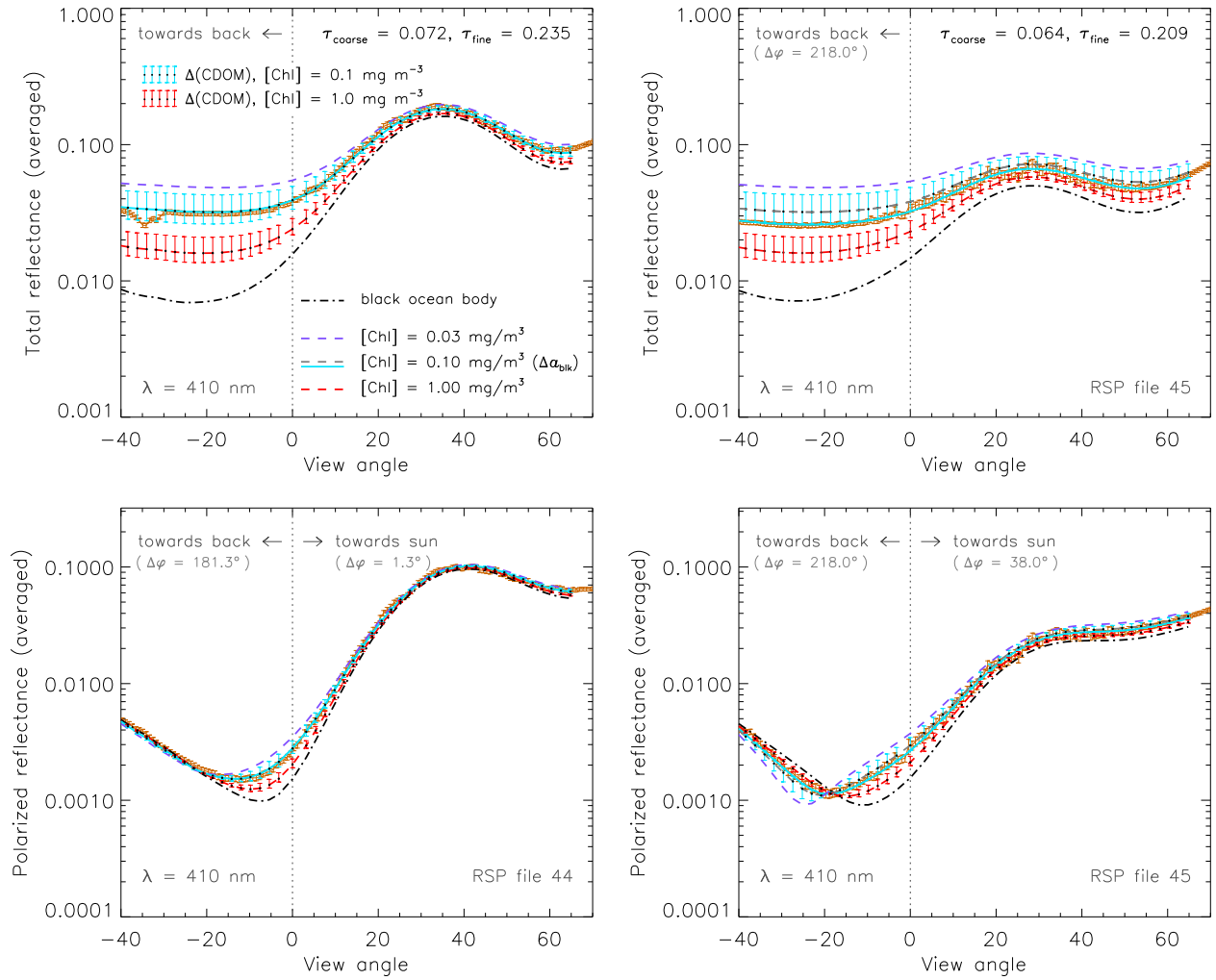


Fig. 11. Analyses of RSP file 44 data (left column) and of RSP file 45 data (right column) obtained at a relative azimuth angle $\Delta\varphi \equiv \varphi - \varphi_0$ of 1.3° and 38° for positive view angle θ , respectively, and at an aircraft altitude z of $65 (\pm 3)$ m. Upper and lower panels are for total reflectance ρ_{tot} and polarized reflectance ρ_{pol} , respectively, at $\lambda = 410$ nm. Yellow lines denote the mean of RSP data, and yellow error bars their standard error ε , as a function of θ . The legend for the corresponding RT results is given in the upper left panel.

of plankton particles instead of D–P matter, is shown as yellow circles. Note that this difference is negative because of a decrease in backscattering ratio q_p , and that it also remains less than ε for all 4 RSP files. The same is true for other $[\text{Chl}] \leq 1.0 \text{ mg/m}^3$ (results not shown here). This figure therefore confirms that for low- or mid-altitude observations, variations in CDOM and in hydrosol scattering matrix of the type that are considered in this work play a minor role in the analyses of polarized reflectance from measurements over open oceans compared to changes in $[\text{Chl}]$ itself, as long as $[\text{Chl}] \leq 1.0 \text{ mg/m}^3$.

5.3.2. Spaceborne polarized reflectance

In Fig. 13, we examine various changes in the top-of-atmosphere (TOA) polarized reflectance. The specifications for the viewing geometry and AOS are the same as the ones for the reflectance fit of RSP file 55. The panels in the upper row of Fig. 13 are for $\lambda = 410$ nm and 443 nm, and in the lower row for 470 nm and 550 nm. Together, they cover the visible bands monitored by RSP and APS. Shown in each panel are the measurement uncertainty κ for the TOA polarized reflectance (grey error bars), and the contribution to κ of the calibration uncertainty ζ (purple error bars) and of the polarization uncertainty η (green error bars). In what follows, we assume that TOA observations are not averaged over consecutive scans in which case κ becomes the standard error ε as well. For the lower half of each panel that we assume $\zeta = 3.0\%$ which is representative for the pre-

launch calibration uncertainty estimate of Earth-observing satellite instruments (e.g., Bruegge et al., 1998), whereas for the upper half of each panel we use $\zeta = 1.5\%$ which is representative of the uncertainty for on-orbit cross calibration of Earth-observing satellite instruments (e.g., Eplee et al., 2011). We remark that pre-launch calibration uncertainties can increase to $\zeta \geq 4.0\%$ after transfer to orbit due to changes in calibration procedure (e.g., Barnes et al., 2000) and to degradation in sensor response (e.g., Bruegge et al., 2007). On the other hand, carefully-designed vicarious calibration experiments lead to $\zeta < 1.0\%$ for the retrieval of water-leaving radiance (Eplee et al., 2001). Hence our ζ values cover a conservative range of calibration uncertainties, and Fig. 13 shows that they dominate the measurement uncertainty κ if we choose for η the RSP polarization uncertainty 0.002 (η becomes the dominant term in the measurement uncertainty κ for the majority of viewing angles in Fig. 13 if $\eta \geq 0.004$ for $\zeta \geq 1.5\%$, or $\eta \geq 0.008$ for $\zeta \geq 3.0\%$). The open circle symbols in Fig. 13 further show changes in TOA polarized reflectance that are caused by variations in K_{bio} for $[\text{Chl}] = 1.0 \text{ mg/m}^3$. Note from the discussion in Section 5.1 that these variations are dominated in the blue part of the spectrum by the natural variability in CDOM absorption, and that they decrease in magnitude with decreasing $[\text{Chl}]$. The corresponding change in TOA polarized reflectance remains, according to Fig. 13, well within the measurement uncertainty κ (it will become larger than κ only if $\zeta \leq 0.5\%$ for $\eta = 0.002$). This extends the

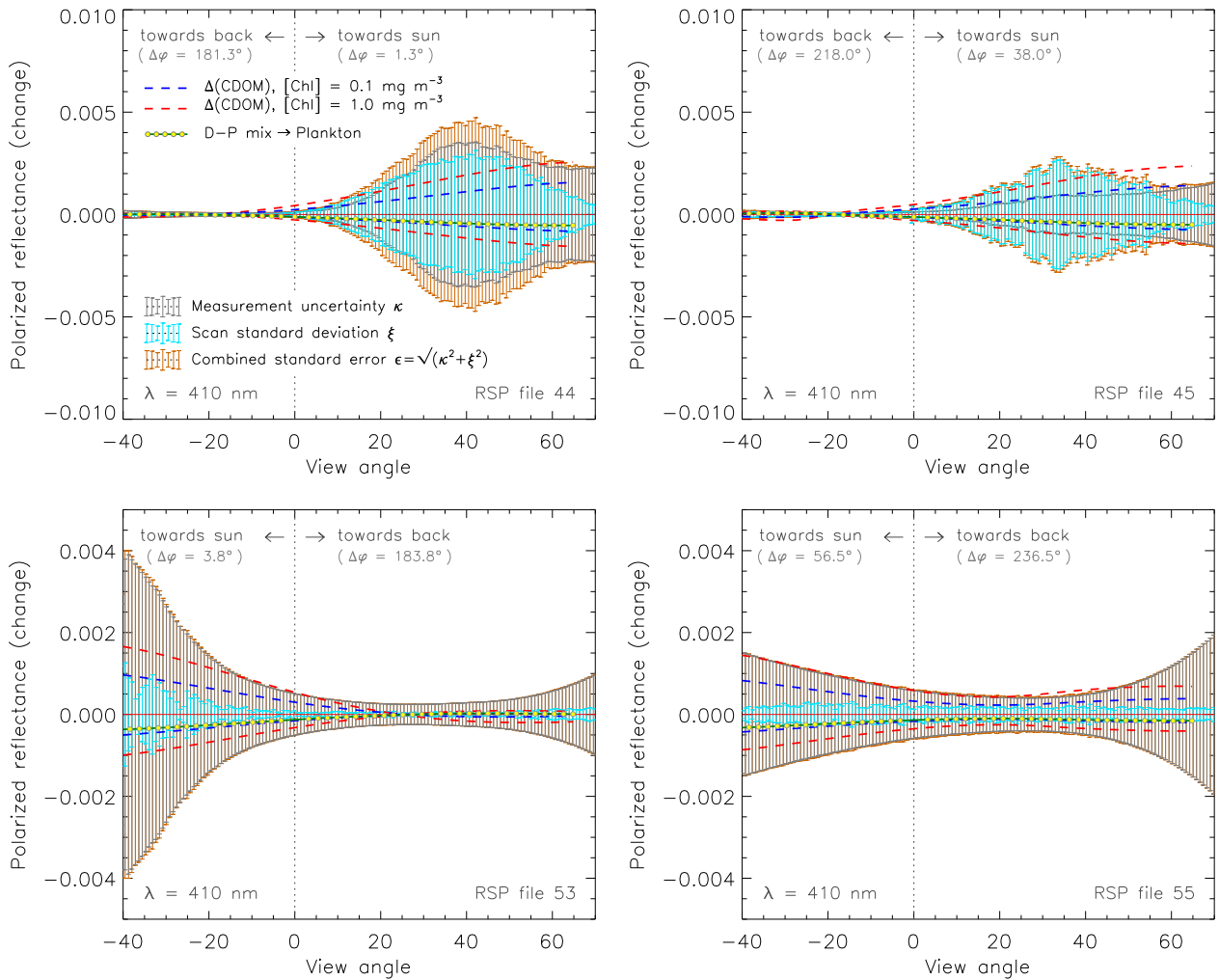


Fig. 12. Isolated uncertainties in RSP polarized reflectance (error bars), and isolated changes in RT polarized reflectance with CDOM and particulate matter (dashed lines), as a function of viewing angle θ . Panels are for RSP files 44 (upper left), 45 (upper right), 53 (lower left), and 55 (lower right) at $\lambda = 410$ nm. The legend for the RSP and RT results is given in the upper left panel.

conclusions drawn for the impact of CDOM variations on RSP data in Section 5.3.1 to APS-like observations from space. Finally, we consider in Fig. 13 changes in the TOA polarized reflectance that are caused by variations in [Chl]. The blue, green, and red dashed lines show the difference in TOA polarized reflectance if [Chl] increases from a base value of 0.03 mg/m^3 to 0.1 mg/m^3 , 0.3 mg/m^3 , and 1.0 mg/m^3 , respectively. Note that these differences change sign between $\lambda = 470$ nm and 550 nm because of a transition from an underwater light scattering regime in the blue part of the spectrum that is impacted by a plankton absorption peak, to an underwater light scattering regime in the green part of the spectrum that is dominated by particulate backscattering (Nobileau & Antoine, 2005). Within this spectral transition, the water-leaving radiance becomes least sensitive to variations in [Chl] at $\lambda \approx 510$ nm (see also A_{blk} spectra in Fig. 3a). The corresponding change in TOA polarized reflectance is negligible at this wavelength (not shown), and Fig. 13 shows that it remains small for larger wavelengths up to $\lambda = 550$ nm. However the reflectance change with [Chl] becomes prominent for $\lambda \leq 470$ nm and can exceed the measurement uncertainty κ even if $\zeta = 3.0\%$. Table 6 tabulates the corresponding TOA polarized reflectance change for Fig. 13 averaged over the entire viewing range. For comparison, we included also cases for a purely molecular atmosphere. It is clear from this table that the TOA polarized reflectance is less sensitive to variations in [Chl], and therefore less suitable for the retrieval of [Chl], than the

TOA total reflectance. Nevertheless, the scan-average TOA polarized reflectance change with [Chl] remains larger than κ for a variety of atmospheres, ζ and [Chl] variations. For example, it becomes more than 6% of the TOA polarized reflectance for a molecular atmosphere at $\lambda = 410$ nm if [Chl] increases from 0.03 mg/m^3 to 1.0 mg/m^3 . Furthermore, the scan-average values in Table 6 underestimate the maximum effect on TOA polarized reflectance of changing [Chl] as this effect varies with viewing angle. We therefore conclude that variations with [Chl] in TOA polarized reflectance observed over open ocean by APS-like polarimeters cannot be ignored if $\lambda \leq 470$ nm. The validity of these model calculations is underpinned by the validation of our RT code against a completely independent method (Zhai et al., 2010), by the match of our RT results for the spectral and angular variation of the reflectance and polarized reflectance to RSP measurements just above the ocean surface, and by the consistency of our retrieved model parameters with those retrieved from MODIS/Aqua (Moore et al., 2009).

It is worthwhile to compare our results with those of Harmel and Chami (2008) (henceforth referred to as HC2008) who also investigated changes in TOA polarized reflectance with [Chl]. To put the comparison in proper context, we remark that our model computations, scope of study, and measurement uncertainties κ differ from those of HC2008. That is, their model computations are performed for oceanic waters where the particulate matter consists of plankton particles only and where the presence of CDOM can be ignored. This

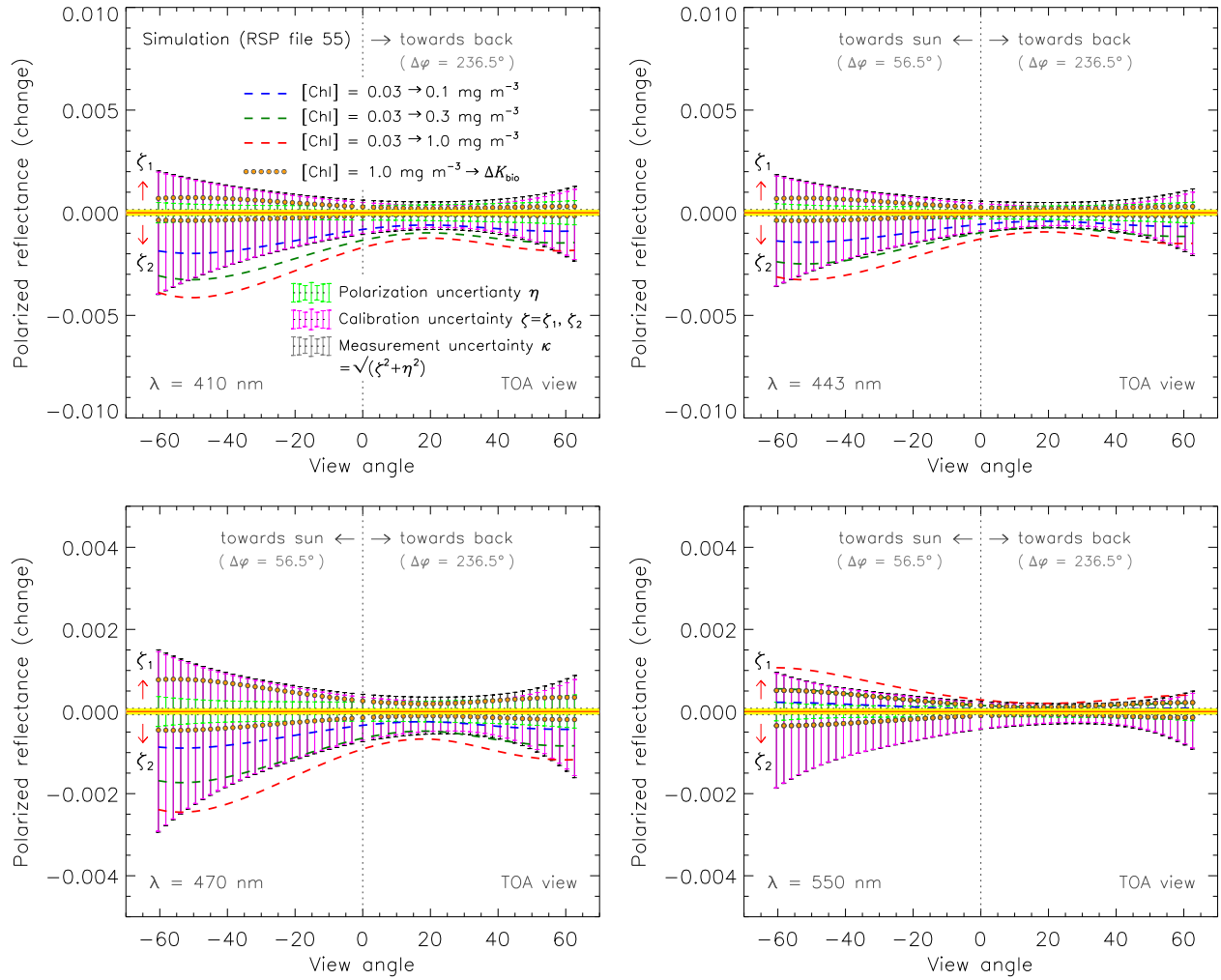


Fig. 13. Isolated uncertainties in APS-like polarized reflectance (error bars), and corresponding isolated changes in RT polarized reflectance with [Chl] (dashed lines) and K_{bio} (open circles), as a function of viewing angle θ . Panels are for the atmosphere–ocean system of RSP file 55 at $\lambda = 410 \text{ nm}$ (upper left), 443 nm (upper right), 470 nm (lower left), and 550 nm (lower right). Upper and lower half of each panel assume the radiometric calibration uncertainty $\zeta_1 = 1.5\%$ and $\zeta_2 = 3.0\%$, respectively, whereas the polarization uncertainty η remains 0.002 for both halves. The legend for the RT results is given in the upper left panel.

leads to ocean colors that follow the A_{blk} spectra shown by the solid black circles in Fig. 4a – but the polarized reflectance should be less affected by these model differences as shown by Fig. 12 (although we did not consider oceans without CDOM in that figure). HC2008 further focus the *scope* of their study on data obtained by the POLDER instrument onboard the Polarization and Anisotropy of Reflectance for Atmospheric Sciences coupled with Observations from a Lidar (PARASOL) mission (Fougnie et al., 2007). This confines their polarized reflectance analyses to one wavelength in the visible part of

the spectrum, viz. $\lambda = 490 \text{ nm}$. Finally, they adopt for their *data uncertainty* an estimate of the instrumental noise for POLDER observations of ocean targets that is 4×10^{-4} and 8.5×10^{-4} for total and polarized reflectance observations, respectively. Under these conditions, and choosing for our TOA computations the same viewing geometry and atmosphere as for RSP file 55, we are able to reproduce their RT results – namely, that the maximum change in polarized reflectance observed from space over open ocean at $\lambda = 490 \text{ nm}$ remains well below their noise-equivalent reflectance values if [Chl] varies within

Table 6

Simulated change with [Chl] in reflectance, evaluated at top of the atmosphere and averaged over a scan of $-60^\circ \leq \theta \leq 60^\circ$, for ground track and solar angle of RSP file 55. The atmosphere contains either the aerosol modes for RSP file 55 (reflectance change shown in normal font) or no aerosol at all (reflectance change shown in italic font). The change, given both in absolute units and in percent, is relative to the case with smallest [Chl].

ρ	$\Delta[\text{Chl}]^a$	$\lambda = 410 \text{ nm}$	$\lambda = 443 \text{ nm}$	$\lambda = 470 \text{ nm}$	$\lambda = 490 \text{ nm}$	$\lambda = 550 \text{ nm}$
ρ_{pol}	0.03 → 1.0	-2.6×10^{-3} (4.6%)	-2.0×10^{-3} (4.0%)	-1.5×10^{-3} (3.9%)	-8.3×10^{-4} (2.5%)	5.7×10^{-4} (2.3%)
		-3.8×10^{-3} (6.1%)	-2.8×10^{-3} (5.4%)	-2.1×10^{-3} (5.2%)	-1.1×10^{-3} (3.4%)	7.2×10^{-4} (3.3%)
	0.1 → 1.0	-1.4×10^{-3} (2.4%)	-1.1×10^{-3} (2.3%)	-9.7×10^{-4} (2.5%)	-6.0×10^{-4} (1.8%)	4.5×10^{-4} (1.8%)
		-1.9×10^{-3} (3.2%)	-1.6×10^{-3} (3.1%)	-1.3×10^{-3} (3.4%)	-7.9×10^{-4} (2.5%)	5.7×10^{-4} (2.6%)
ρ_{tot}	0.03 → 1.0	-2.3×10^{-2} (11%)	-1.6×10^{-2} (8.9%)	-1.1×10^{-2} (7.6%)	-5.6×10^{-3} (4.7%)	2.6×10^{-3} (3.5%)
		-2.6×10^{-2} (14%)	-1.8×10^{-2} (12%)	-1.2×10^{-2} (11%)	-6.3×10^{-3} (6.8%)	2.8×10^{-3} (5.6%)
	0.1 → 1.0	-1.1×10^{-2} (5.6%)	-8.6×10^{-3} (5.0%)	-6.6×10^{-3} (5.0%)	-4.0×10^{-3} (3.5%)	2.1×10^{-3} (2.8%)
		-1.3×10^{-2} (7.3%)	-9.7×10^{-3} (6.7%)	-7.5×10^{-3} (6.9%)	-4.5×10^{-3} (5.0%)	2.3×10^{-3} (4.5%)

^a [Chl] change in mg m^{-3} .

0.03 and 3.0 mg/m^3 . HC2008 do not provide RT results for the accompanying change in total reflectance, but from Fig. 4a (solid black circles) we observe that the corresponding A_{blk} spectra exhibit as well negligible sensitivity to [Chl] at 490 nm. If we consider oceans containing D–P matter for our computations then we can also reproduce the HC2008 POLDER data analyses reasonably well. That is, the RT results in Table 6 for $\lambda = 490 \text{ nm}$ show a corresponding decrease in TOA total and polarized reflectance, the average of which (over the entire angular range) is 4.0×10^{-3} and 6.0×10^{-4} respectively as [Chl] increases from 0.1 to 1.0 mg/m^3 . The root-mean-square differences found by HC2008 in POLDER images of two targets in the Mediterranean Sea with similarly differing amounts of [Chl] were 6.7×10^{-3} and 6.2×10^{-4} for unpolarized (\approx total) and polarized reflectance, respectively. The comparison for the change in TOA polarized reflectance is excellent in spite of this change being smaller than the estimated instrumental noise in POLDER observations. The change in TOA total reflectance for the POLDER data is large, surpassing even the scan-average change in our RT results for a purely molecular atmosphere (i.e., 4.5×10^{-3} from Table 6). However, in situ measurements of a_{blk} and b_p for the Mediterranean Sea exhibit systematic anomalies (Claustre et al., 2002; Morel et al., 2007) that are not accounted for in our bio-optical model. Hence, it is reasonable for the change in TOA total reflectance calculated from our model and observed by POLDER to differ given the modeling uncertainty induced by these anomalies. Our RT computations in Table 6 show further that the scan-average change with [Chl] of TOA polarized reflectance remains within 8.5×10^{-4} for $\lambda = 550 \text{ nm}$ even if the atmosphere is purely molecular and/or [Chl] increases from 0.03 mg/m^3 to 1.0 mg/m^3 . However, the results in Table 6 also show that variations with [Chl] of TOA polarized reflectance cannot anymore be ignored if $\lambda \leq 470 \text{ nm}$.

5.3.3. Azimuthal variations

In Figs. 14 and 15, we explore the change with [Chl] of RSP-like reflectance for the entire range of azimuth angle $\varphi - \varphi_0$. The panels in Fig. 14 show polar angle diagrams of such reflectance for the AOS model of RSP file 44 analyses and viewing from an altitude of 65 m. Fig. 15 shows the same diagrams except for viewing this AOS from an altitude of 4.1 km. Note that the reflectance in these diagrams is normalized by its maximum value ρ_{max} for the given range of polar angles. The polar viewing angle θ is shown in units of $\mu \equiv \cos \theta$ and ranges from $\mu = 1$ ($\theta = 0^\circ$) at the center point of each diagram to $\mu = 0.5$ ($\theta = 60^\circ$) at the circumference of each diagram, whereas the polar azimuth angle $\varphi - \varphi_0$ increases clockwise from 0° (specular direction) to 180° (backscattering direction) to 360° for each diagram. The corresponding value of ρ_{max} is given in the lower right corner of each diagram. The left two columns in Figs. 14 and 15 show the normalized total reflectance, and the right two columns the normalized polarized reflectance, for an AOS whose ocean body is either completely absorbing (first row) or contains D–P matter with [Chl] = 0.03 mg/m^3 (second row) or [Chl] = 1.0 mg/m^3 (third row). The wavelength for the reflectance is shown at the bottom of each column and is either 410 nm or 550 nm. To visualize the bidirectional changes that occur when varying the ocean body, we overlaid the normalized polarized reflectance diagrams for [Chl] = 0.03 mg/m^3 (see second row) and 1.0 mg/m^3 (see third row) with white contour lines depicting the minima for the case of a black ocean (from first row). In addition, we provide the downwind direction (see orange line) of the ocean surface wind that reproduces the cross section of the reflectance in the sunglint for RSP file 44 at $\lambda = 2250 \text{ nm}$, and show the orientation of the ground tracks (see purple dashed lines) for RSP files 45 and 55 for the low- and mid-altitude simulations, respectively. A yellow star locates the anti-solar position of the sun which is at $\varphi - \varphi_0 = 180^\circ$ and $\mu_0 = 0.85$ ($\theta_0 = 32^\circ$) for all diagrams. The information displayed in Figs. 14 and 15 provides a more general context for the snapshots captured by RSP files 44, 45, 53, and 55 in Figs. 5–8. The most prominent features are

the modeled sunglint profile, and we observe that the wind-directionality of the ocean surface roughness causes this profile to be asymmetric with respect to the solar principal plane. The downwind direction estimated from the RSP observations of sunglint varies between the RSP files, and this causes the modeled sunglint profile for RSP files 45 to 55 to differ from the one shown in Figs. 14 and 15. Nevertheless, the reflectance generated by sunglint becomes small-to-negligible beyond the azimuth angle range of $-60^\circ < \varphi_0 - \varphi < 60^\circ$ because of the moderate ocean surface wind speeds. Note that the ground track for RSP file 55 is at the edge of this range and the reflectance in this file is therefore least affected by fluctuations in the sunglint. This is evident in the small scan-to-scan standard error values in the sunglint region of Fig. 12. Such weak sunglint signals cause the ocean surface wind retrieved from the 2250 nm reflectance in such geometries to be less accurate, but this does not affect aerosol and ocean color estimates precisely because the glint contributions are so small. At this point, we remark that sunglint signals were also used in the analyses of RSP reflectance to validate measurements of the aircraft attitude (i.e., roll, pitch, and yaw) angles. These angles are vital to the correction of viewing geometry for aircraft attitude, but their measurements were at times not accurate enough (i.e., not within a few tenths of degree) to resolve rapid changes of the polarized reflectance with viewing geometry. Sunglint profiles are unique and vary in a predictable way with the ocean surface wind, which makes them excellent targets for validating aircraft attitude angles in addition to retrieving wind speeds. Clearly, a weak sunglint signal such as that contained by RSP file 55 limits the efficacy of this validation. Another prominent feature in Figs. 14 and 15 is the appearance of a neutral point in the polarized reflectance on either side of the solar principal plane. Such points have been recorded in airborne POLDER images of the Mediterranean Sea (Kawata & Yamazaki, 1998) and more recently in images of upwelling polarized radiance just below the surface in clear waters off the coast of Hawaii (Voss et al., 2011). They occur, according to Eq. (26), at viewing geometries where Stokes parameters Q and U of the measured light become both zero. Simulations performed by Adams and Kattawar (1997) show that including hydrosols in the ocean affects this occurrence for the upwelling polarized light in atmosphere–ocean systems. The neutral points of such light should therefore vary in position with [Chl], and this can be seen in Figs. 14 and 15 by the change in bidirectionality when compared to the white contour lines. The location of the neutral point at 410 nm differs from that for a black ocean body more for [Chl] = 0.03 mg/m^3 than for [Chl] = 1.0 mg/m^3 . This is because of the large contribution to the polarized water-leaving radiance of Rayleigh-Brillouin scattering at a wavelength of 410 nm for low [Chl]. The opposite is true at $\lambda = 550 \text{ nm}$, but the differences here are much smaller because of the decrease in spectral sensitivity to [Chl] of polarized reflectance (cf. Fig. 9). Note that the ground track of RSP file 45 crosses a neutral point whereas that for RSP file 55 only grazes a neutral point. This explains the large variation seen in the RT model simulations (Fig. 6, $\lambda = 410 \text{ nm}$) for the polarized reflectance of file 45 and makes the model match to RSP reflectance in this figure a particularly robust validation of the model.

6. Summary

In a previous paper (Chowdhary et al., 2006), we developed a variable detritus-plankton (D–P) hydrosol model to compute the multi-angle and multi-spectral behavior of polarized light emerging from open oceans as a function of Chlorophyll *a* concentration [Chl]. The purpose of that model was to account for the polarized underwater light contribution to measurements made by spaceborne polarimeters. In this work, we reviewed the properties of this hydrosol model and made a correction for the spectral behavior of the particulate scattering coefficient b_p and backscattering efficiency q_p . We then perturbed this model to examine the radiative transfer (RT) effects on underwater light irradiance ratio A_{blk} of variations in the

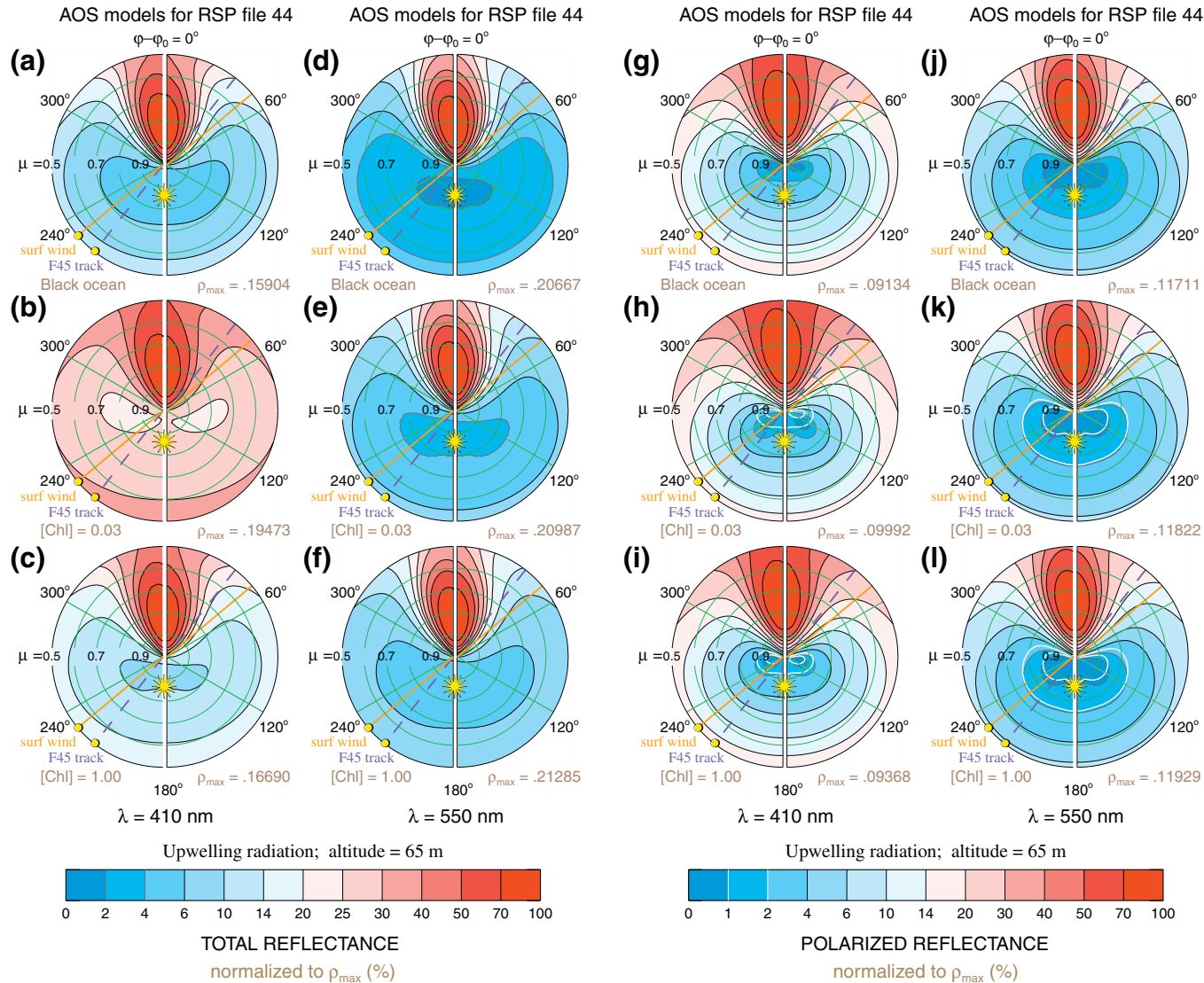


Fig. 14. Polar diagrams of total reflectance ρ_{tot} (left two columns) and polarized reflectance ρ_{pol} (right two columns) normalized by their maximum value ρ_{max} , respectively. The results are computed for the AOS model of RSP file 44 analyses, and for viewing from an altitude z of 65 m. The ocean body is either completely absorbing (first row), or contains D–P matter with $[\text{Chl}] = 0.1 \text{ mg/m}^3$ (second row) or $[\text{Chl}] = 1.0 \text{ mg/m}^3$ (third row). The wavelength λ is 410 nm for diagrams (a)–(c) and (g)–(i), and 550 nm for diagrams (d)–(f) and (j)–(l). A yellow star locates the antisolar point, and the yellow dots provide the azimuth angle of the aircraft heading for RSP file 45 (depicted by the purple line) and of the ocean surface downwind (depicted by the orange line). The white lines in diagrams (h)–(i) show the 1% and 2% contours of diagram (g), and the white lines in diagrams (k)–(l) the 1% and 2% contours of diagram (j). (For interpretation of the color references in this figure legend, the reader is referred to the web version of this article).

absorption coefficient a_{blk} caused by colored dissolved organic matter (CDOM) anomalies, and in the bulk ocean backscattering coefficient s_{blk} caused by changes in the scattering function of marine particulates.

Next, we applied the D–P hydrosol model to the analyses of data obtained during the MILAGRO/INTEX-B campaign in March of 2006 by the RSP (Cairns et al., 1999) which is an airborne version of the satellite polarimeter instrument APS (Peralta et al., 2007). Flights were conducted over a patch of open ocean off the coast of Veracruz (Mexico) at low (65 m) and mid (4.1 km) altitudes, and at azimuth angles close to the solar principal plane (i.e., less than 4° away) and away from this plane (i.e., between 38° and 57° away), to capture the spectrum and bidirectionality of polarized water leaving radiances and to study their contribution to RSP measurements. We focused our analyses on RSP measurements made at wavelengths $\lambda = 410$ and 550 nm, and conducted RT studies to investigate the sensitivity of these measurements to variations in $[\text{Chl}]$, a_{blk} and s_{blk} . We also investigated the sensitivity of APS-like polarized reflectance measurements to variations in $[\text{Chl}]$ and a_{blk} at $\lambda = 410$, 443 , 470 and 550 nm. The range for $[\text{Chl}]$ in these studies was restricted to $0.03 \text{ mg/m}^3 \leq [\text{Chl}] \leq 1.0 \text{ mg/m}^3$.

The analyses of airborne reflectance measurements yielded the following results. The *polarized* reflectance obtained over open oceans by an RSP-like instrument is sensitive to variations in polarized water-leaving radiance with $[\text{Chl}]$. The magnitude of these variations depends on the wavelength, on the base value of $[\text{Chl}]$, and on the viewing geometry – but the scaling factor for the differences in polarized reflectance does not depend notably on the viewing geometry. The variations become largest at $\lambda = 410$ nm, at azimuth planes away from the solar principal plane, and for perturbations in $[\text{Chl}]$ from a base value of 0.03 mg/m^3 . Under these conditions, and excluding neutral polarization points, the resulting variation in RSP polarized reflectance exceeds the standard error ε for this reflectance by a factor of up to 2 for low- and mid-altitude observations if $[\text{Chl}]$ increases to 0.1 mg/m^3 . On the other hand, increasing the base value of $[\text{Chl}]$ to 1.0 mg/m^3 , or approaching the solar principal plane to within a few degrees, causes the variation in RSP polarized reflectance with $[\text{Chl}]$ to approach ε for the same relative change in $[\text{Chl}]$. All actual RSP polarized reflectance measurements in this work are matched for $[\text{Chl}] = 0.1 \text{ mg/m}^3$ at $\lambda = 410$ nm. At $\lambda = 550$ nm the polarized RSP reflectance is relatively insensitive to variations in $[\text{Chl}]$ for low and mid altitudes, for small and large azimuth angles, and for small and large base values of $[\text{Chl}]$. However, the contribution of ocean body scattering to polarized reflectance observed at large azimuth angle does need to be properly accounted for at this wavelength even though the dependence on $[\text{Chl}]$ is negligible.

The *total* reflectance observed over open oceans by an RSP-like instrument exhibits, as expected, large sensitivity to variations in total water-leaving radiance with $[\text{Chl}]$. These variations depend on the wavelength and on the base value of $[\text{Chl}]$ similar to those of polarized water-leaving radiance, but their magnitude is much larger and their dependence on the viewing geometry much weaker. At $\lambda = 410$ nm and perturbing $[\text{Chl}]$ from a base value of 0.03 mg/m^3 , they cause the off-sunglint RSP total reflectance to vary by several factors of ε for low- and mid-altitude observations if $[\text{Chl}]$ increases to 0.1 mg/m^3 , and by at least an order of magnitude of ε if $[\text{Chl}]$ approaches 1.0 mg/m^3 . Taking a base value of 1.0 mg/m^3 for $[\text{Chl}]$ reduces the variation of RSP total reflectance with $[\text{Chl}]$, but it still remains larger than ε if $[\text{Chl}]$ decreases to 0.3 mg/m^3 . At $\lambda = 550$ nm, the sensitivity of total RSP reflectance to variations in $[\text{Chl}]$ is smaller but it still exceeds ε if $[\text{Chl}]$ increases from 0.03 to 0.3 mg/m^3 , or if it decreases from 1.0 to 0.3 mg/m^3 . We remark that all actual RSP total reflectance measurements considered in this work are matched at $\lambda = 550$ nm for $[\text{Chl}] = 0.1 \text{ mg/m}^3$, but the ones at $\lambda = 410$ nm require an additional perturbation in a_{blk} for some flight tracks. These perturbations are however consistent with variations in the diffuse attenuation

coefficient K_d values retrieved from MODIS imagery for these flights.

The remaining RT studies yield for blue light ($\lambda \leq 470$ nm) the following results. Averaging the change in polarized reflectance with $[\text{Chl}]$ over viewing angle for multiangle remote sensing over oceans provides a low estimate for the maximum effect of ocean body scattering. This estimate approaches 4% for spaceborne observations at $\lambda = 470$ nm over open oceans and moderate aerosol burdens, and becomes larger with decreasing wavelength and/or decreasing aerosol optical depth, as $[\text{Chl}]$ increases from 0.03 to 1.0 mg/m^3 . Hence, changes in $[\text{Chl}]$ must be considered in APS-like polarized reflectance analyses for $\lambda \leq 470$ nm. Opposite conclusions are drawn for the variation with CDOM in RSP and APS-like polarized reflectance. That is, using the root-mean-square error in K_{bio} to approximate CDOM-induced variations in a_{blk} , we show that the RT variation in RSP polarized reflectance remains comparable to or smaller than ε at $\lambda = 410$ nm provided that $[\text{Chl}] \leq 1.0 \text{ mg/m}^3$. Simulations for APS-like observations indicate that the space-borne polarized reflectance remains insensitive to variations in CDOM for $\lambda \leq 470$ nm and $[\text{Chl}] \leq 1.0 \text{ mg/m}^3$ even if these observations are vicariously calibrated. At the same time, we confirm that such variations affect the RSP total reflectance by an amount much larger than ε at $\lambda = 410$ nm. This explains why we require perturbations in a_{blk} to fit the RSP total reflectance but not the RSP polarized reflectance. Finally, performing RT computations with Fournier-Forand (FF) or one-term Henyey-Greenstein (OTHG) scattering functions leads to negligible changes in A_{blk} values at $\lambda \leq 470$ nm, and a slight decrease in RSP total reflectance at $\lambda = 410$ nm, provided that these functions retain same the backscattering efficiency q_p as the D–P model. However, the corresponding RSP polarized reflectance decreases significantly because these functions do not account for the polarization of particulate scattering. Conversely, substituting the D–P scattering matrix with a fixed plankton-only scattering matrix accounts for this polarization but not for the variation in q_p . The computations for the latter matrix lead to larger decreases in A_{blk} values at $\lambda \leq 470$ nm, but a negligible decrease in RSP polarized reflectance at $\lambda = 410$ (not shown).

The corresponding RT results for $\lambda \geq 490$ nm are as follows. The scan-angle averaged change with $[\text{Chl}]$ in polarized reflectance is less than 3.5% for space-borne observations over open oceans at $\lambda = 490$ nm, assuming a purely molecular atmosphere and increasing $[\text{Chl}]$ from 0.03 to 1.0 mg/m^3 . This change becomes even smaller when including aerosols and/or increasing wavelength, and can therefore be *ignored* in APS-like polarized reflectance analyses for $\lambda = 550$ nm and $[\text{Chl}] \leq 1.0 \text{ mg/m}^3$. Note further that the natural variation in RSP total and polarized reflectance caused by CDOM remains always smaller than the change in these reflectances caused by increasing $[\text{Chl}]$ from 0.03 to 1.0 mg/m^3 . In addition the contribution to a_{blk} by CDOM decreases rapidly with wavelength, such that it can be ignored at $\lambda = 550$ nm for $[\text{Chl}] \leq 3.0 \text{ mg/m}^3$. We confirmed that excluding CDOM causes a minor-to-negligible increase in A_{blk} at $\lambda \geq 500$ nm, and assume the same to be true for RSP and for APS-like polarized reflectance at $\lambda = 550$ nm, for $[\text{Chl}] \leq 1.0 \text{ mg/m}^3$. Finally, replacing the D–P scattering matrix by a plankton-only scattering matrix, or even by FF or OTHG scattering function, barely affects the polarized reflectance for similar reasons. That is, the resulting RT change in RSP polarized reflectance is negligibly small for all these cases, in part because of the small sensitivity of this reflectance to any change in underwater light scattering at $\lambda = 550$ nm for $[\text{Chl}] \leq 1.0 \text{ mg/m}^3$. Also, RT computations for the FF and OTHG functions show modest-to-negligible changes in A_{blk} values (at $\lambda \geq 500$ nm) and RSP total reflectance (at $\lambda = 550$ nm) provided that these functions retain the same q_p values as the D–P model. However, RT computations for the plankton-only scattering matrix now show large decreases A_{blk} values (at $\lambda \geq 500$ nm) that cannot be ignored if $0.1 \text{ mg/m}^3 \leq [\text{Chl}] \leq 1.0 \text{ mg/m}^3$. For future work, we remark for observations over open oceans at $\lambda = 550$ nm that the variation with $[\text{Chl}]$

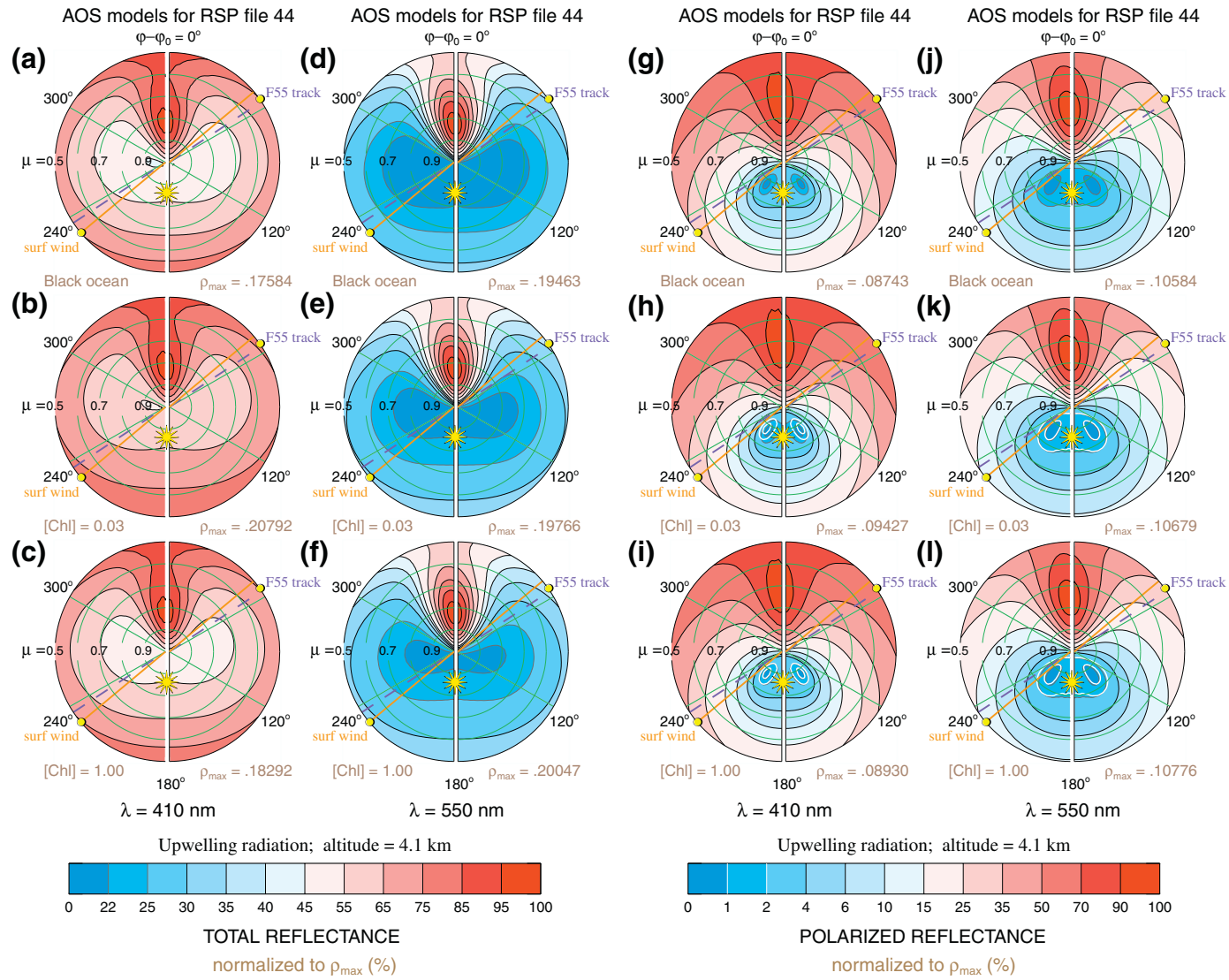


Fig. 15. Same as Fig. 14 except for viewing from an altitude of 4.1 km, and for the yellow dot at the end of the purple line denoting the azimuth angle of the aircraft heading for RSP file 55. (For interpretation of the color references in this figure legend, the reader is referred to the web version of this article).

and CDOM of RSP and APS-like total reflectance increases substantially if $[\text{Chl}] \gg 1.0 \text{ mg/m}^3$. In addition, the natural variability of A_{blk} with the particulate scattering coefficient b_p becomes substantial for $[\text{Chl}] \gg 1.0 \text{ mg/m}^3$. For observations over such oceans, the variation of RSP and APS-like polarized reflectance with $[\text{Chl}]$, CDOM and b_p remains to be analyzed.

In summary, we conducted RT studies of polarized water-leaving radiance with an updated hydrosol model, validated its results with multispectral and multiangle airborne measurements of polarized reflectance, and applied the results to spaceborne observations, to conclude the following for visible wavelengths. Polarized water-leaving radiance varies with the wavelength of light, with the viewing geometry of the observations, and with the biomass in the ocean. The sensitivity of remotely sensed polarized reflectance to these variations is smallest for mid-altitude observations near the solar principal plane, and vanishes in the vicinity of the backscattering direction, regardless of λ and $[\text{Chl}]$. Satellites rarely encounter such viewing geometries, but some simplifications remain. Firstly, polarized reflectance observed from space at $\lambda > 470 \text{ nm}$ is sensitive to the contribution of water-leaving radiance, but its variation with $[\text{Chl}]$ and CDOM can be ignored for $[\text{Chl}] \leq 1.0 \text{ mg/m}^3$. Second, polarized reflectance observed from space at $\lambda \leq 470 \text{ nm}$ is sensitive both to the contribution of water-leaving radiance and to the variations in $[\text{Chl}]$, but its variation with CDOM remains minor, for $[\text{Chl}] \leq 1.0 \text{ mg/m}^3$. Finally, polarized reflectance observed from space is rather insensitive to variations in particulate scattering provided that the polarization of this scattering is accounted for, and that the particulate backscattering efficiency b_p remains the same. The above mentioned validation and sensitivities of remotely sensed polarized reflectance need to be re-examined in a future work for open oceans with $[\text{Chl}] \gg 1.0 \text{ mg/m}^3$.

Acknowledgements

The MILAGRO/INTEX-B Campaign is a collaborative effort of a large number of participants with the support of multi-national agencies. We thank the governments of the Federal District, the States of Mexico, Hidalgo and Veracruz, and the Mexican Ministries of the Environment, Foreign Relations, Defense and Finance for their logistical support; IMP, U-Tecamac, and Rancho La Bisnaga for hosting the supersites; and many other Mexican institutions for their support. We further extend our gratitude to all MILAGRO/INTEX-B participants and sponsoring agencies who made this research possible. We appreciate the fruitful discussions with Emmanuel Boss and Dave Siegel on the spectrum of underwater light particulate backscattering and on CDOM variations, and with André Morel and Stéphane Maritorena on the implementation of these quantities, on variations of particulate scattering functions with $[\text{Chl}]$, and on variations of underwater light fluxes with solar zenith angles. We are further grateful for the kernels provided by Oleg Dubovik to compute scattering matrices of randomly oriented spheroid aerosols, for the comments by Tatyana Lapyonok on using these kernels, and for the spectra provided by Annick Bricaud for absorption by marine particulates. We also thank Tristan Harmel for useful comments on an earlier draft of this manuscript, and the anonymous reviewers for their constructive comments on the submitted manuscript. The mission scientist for the J31 was Phillip Russel to whom we express our deep appreciation for the effective and collegial use of flight hours. The J-31 measurements were supported by the NASA Radiation Sciences Program. The MODIS/Aqua ocean color data were obtained from NASA Goddard Space Flight Center. This study was funded by the NASA Glory Mission project and the NASA Radiation Sciences Program managed by Hal Maring.

Appendix A. Corrections for D–P hydrosol mixtures

In their bio-optical model, Morel and Maritorena (2001) derive the bulk ocean backscattering coefficient s_{blk} from the product of

the particulate scattering coefficient b_p and the particulate backscattering efficiency q_p (plus a pure-water term), i.e.,

$$s_{\text{blk}} = 0.5b_w + q_p \times b_p. \quad (27)$$

In Section 2B of C2006, we inadvertently interpreted the spectral variation assigned by Morel and Maritorena (2001) to $q_p \times b_p$ as belonging to q_p . Part of our error resulted from Morel and Maritorena (2001) ascribing in their study a different spectral variation for b_p . Note that adopting a potentially wrong spectral dependence for b_p introduces artificial changes in s_{blk} , which in turn affect the bio-optical computation of the bulk ocean subsurface irradiance ratio A_{blk} following Eq. (11). Our error also affects the radiative transfer computation of A_{blk} by changing F_p in Eq. (13), by changing F_{blk} in Eq. (2), and by changing ω_{blk} in Eq. (3) if a_{blk} is parameterized in terms of A_{blk} as in Morel and Maritorena (2001).

To correct the bio-optical computations of A_{blk} in Section 3B of C2006, we use Eqs. (4)–(6) for b_p and Eq. (14) for q_p that are taken from Huot et al. (2008). The latter work avoids the potential for confusing the spectral variations of b_p and q_p , assigns the same spectral variation to b_p and s_{blk} , and has the additional advantage of actually validating this variation with in situ data. The resulting values for b_p and q_p are listed in Table 2, and differ up to 38% and 20% from those used by C2006 if $[\text{Chl}] = 3.0 \text{ mg/m}^3$ and 0.03 mg/m^3 , respectively. While these differences are substantial, they occur at $\lambda = 410 \text{ nm}$ where the product of b_p and q_p contributes least to s_{blk} because of the relatively large contribution to s_{blk} (by means of $0.5b_w$) of scattering by pure seawater in the blue. This causes the bio-optical computations of A_{blk} in Fig. 3a (solid curves) to change by less than 15%, and those of a_{blk} in Table 2 by (much) less than 5%, for all wavelengths and $[\text{Chl}]$ compared to the values computed in C2006.

The changes in F_{blk} and ω_{blk} caused by the above-mentioned differences in b_p are 0.5% and 7% or less, respectively, compared to C2006. In addition, the values listed for f_{det} in Table 2 differ from those in C2006 by up to 13% if $[\text{Chl}] = 0.03 \text{ mg/m}^3$. This causes an additional change in F_{blk} – but the amount remains relatively small. Nevertheless, the RT computations of A_{blk} shown in Fig. 3a by the circles differ from those in Section 3B of C2006 by up to 28% (for $\lambda = 410 \text{ nm}$ and $[\text{Chl}] = 3.0 \text{ mg/m}^3$). That is amongst others because the number of underwater light scattering events varies as $(1 - \omega_{\text{blk}})^{-1}$ according to Morel and Gentili (1991), which makes A_{blk} particularly sensitive to small changes in ω_{blk} . On the other hand, the bio-optical and RT computations of A_{blk} in Fig. 3a agree now even better than in C2006. Hence, the corrections in b_p and q_p strengthen the arguments in favor of using D–P hydrosol model to analyze polarimetric remote sensing data over open oceans.

Note that while the current changes in b_p and q_p modify the values of A_{blk} computed in Section 3B of C2006, they do not change the scattering properties of the individual particulate components derived for D–P mixtures in Sections 2C and 3A of C2006. In particular, the linear relation between the power law exponent γ for the differential size distribution of oceanic particulates and the refractive index m remains the same, and so do the set of corresponding values in Table 3. Also, the conclusion made in C2006 for high-altitude observations that the bidirectionality of polarized waterleaving radiance shows little variation with $[\text{Chl}]$ for given wavelength and D–P hydrosol mixture remains valid, as is exemplified in Fig. 9 of the current work. Naturally, the magnitude of water leaving radiance computed in C2006 differs from that computed in this work for given wavelength and D–P hydrosol mixture just like the RT computations of A_{blk} discussed above. Finally, three symbols were used in Section 2A of C2006 to represent a small-volume element of the AOS, viz., dV , $d\nu$, and dv . They should all be the same symbol dv .

References

- Adams, J. T., & Kattawar, G. W. (1997). Neutral points in an atmosphere–ocean system. 1: Upwelling light field. *Applied Optics*, 36, 1976–1986.
- Barnes, R. A., Eplee, R. E., Jr., Biggar, S. F., Thome, K. J., Zalewski, E. F., Slater, P. N., et al. (2000). SeaWiFS transfer-to-orbit experiment. *Applied Optics*, 39, 5620–5631.
- Barnes, W. L., Pagano, T. S., & Salmonson, V. V. (1998). Prelaunch characteristics of the Moderate Resolution Imaging Spectrometer (MODIS) on EOS-AM1. *IEEE Transactions on Geoscience and Remote Sensing*, 36, 1088–1100.
- Bergstrom, R. W., Schmidt, K. S., Coddington, O., Pilewskie, P., Guan, H., Livingston, J. M., et al. (2010). Aerosol spectral absorption in the Mexico City area: Results from airborne measurements during the MILAGRO/INTEX B. *Atmospheric Chemistry and Physics*, 10, 6333–6343. doi:10.5194/acp-10-6333-2010.
- Bréon, F. -M., & Goloub, P. (1998). Cloud droplet effective radius from spaceborne polarization measurements. *Geophysical Research Letters*, 25, 1879–1882.
- Bricaud, A., Morel, A., Babib, M., Allali, K., & Claustre, H. (1998). Variations of light absorption by suspended particles with chlorophyll a concentrations in oceanic (case 1) waters: Analysis and implications for bio-optical models. *Journal of Geophysical Research*, 103, 13033–13044.
- Bricaud, A., Morel, A., Babib, M., Allali, K., & Claustre, H. (1999). Erratum: Variations of light absorption by suspended particles with chlorophyll a concentrations in oceanic (case 1) waters: Analysis and implications for bio-optical models. *Journal of Geophysical Research*, 104, 8025.
- Brown, C. A., Huot, Y., Werdell, P. J., Gentili, B., & Claustre, H. (2008). The origin and global distribution of second order variability in satellite ocean color and its potential applications to algorithm development. *Remote Sensing of Environment*, 112, 4186–4203.
- Bruegge, C. J., Diner, D. J., Kahn, R. A., Chrien, N., Helmlinger, M. C., Gaitley, B. J., et al. (2007). The MISR radiometric calibration processes. *Remote Sensing of Environment*, 107, 2–11.
- Bruegge, C. J., Duval, V. G., Chrien, N. L., Korechoff, R. P., Gaitley, B. J., & Hochberg, E. B. (1998). MISR prelaunch instrument calibration and results. *IEEE Transactions on Geoscience and Remote Sensing*, 36, 1186–1198.
- Cairns, B., Travis, L. D., & Russel, E. E. (1999). The Research Scanning Polarimeter: Calibration and ground-based measurements. *Proceedings of SPIE*, 3754, 186–196.
- Cairns, B., Waquet, F., Knobelspiesse, K., Chowdhary, J., & Deuzé, J. -L. (2009). Polarimetric remote sensing of aerosols over land surfaces. In A. A. Kokhanovskii, & G. De Leeuw (Eds.), *Remote sensing over land* (pp. 295–325). : Springer-Praxis Books in Environmental Sciences. doi:10.1007/978-3-540-69397-0_10.
- Chami, M., Santer, R., & Dillegard, E. (2001). Radiative transfer model for the computation of radiance and polarization in an atmosphere–ocean system: Polarization properties of suspended matter for remote sensing. *Applied Optics*, 40, 2398–2416.
- Chowdhary, J., Cairns, B., Mishchenko, M. I., Hobbs, P. V., Cota, G. F., Redemann, J., et al. (2005). Retrievals of aerosol scattering and absorption properties from photopolarimetric observations over the ocean during the CLAMS experiment. *Journal of the Atmospheric Sciences*, 62, 1093–1117.
- Chowdhary, J., Cairns, B., Mishchenko, M. I., & Travis, L. D. (2001). Retrieval of aerosol properties over the ocean using multispectral and multiangle photopolarimetric measurements from the Research Scanning Polarimeter. *Geophysical Research Letters*, 28, 243–246.
- Chowdhary, J., Cairns, B., & Travis, L. D. (2002). Case studies of aerosol retrievals over the ocean from multiangle, multispectral photopolarimetric remote sensing data. *Journal of the Atmospheric Sciences*, 59, 383–397.
- Chowdhary, J., Cairns, B., & Travis, L. D. (2006). Contribution of waterleaving radiances to multiangle, multispectral polarimetric observations over the open ocean: Bio-optical model results for case 1 waters. *Applied Optics*, 45, 5542–5567.
- Claustre, H., Morel, A., Hooker, S. B., Babin, M., Antoine, D., Oubelkheir, K., et al. (2002). Is desert dust making oligotrophic waters greener? *Geophysical Research Letters*, 29, doi:10.1029/2001GL014056.
- Coulson, K. L. (1988). *Polarization and Intensity of Light in the Atmosphere*. Hampton, VA: Deepak.
- Cox, C., & Munk, W. (1954). Statistics of the sea-surface derived from sun-glitter. *Journal of Marine Research*, 13, 198–227.
- de Haan, J. F., Bosma, P. B., & Hovenier, J. W. (1987). The adding method for multiple scattering computations of polarized light. *Astronomy and Astrophysics*, 183, 371–391.
- Deschamps, P. -Y., Breon, F. -M., Leroy, M., Podaire, A., Bricaud, A., Burier, J. -C., et al. (1994). The POLDER mission: Instrument characteristics and scientific objectives. *IEEE Transactions on Geoscience and Remote Sensing*, 32, 598–615.
- Dubovik, O., Sinyuk, A., Lapyonok, T., Holben, B. N., Mishchenko, M., Yang, P., et al. (2006). Application of spheroid models to account for aerosol particle nonsphericity in remote sensing of desert dust. *Journal of Geophysical Research*, 111, D11208. doi:10.1029/2005JD006619.
- Eplee, R. E., Jr., Robinson, W. D., Bailey, S. W., Clark, D. K., Werdell, P. J., Wang, M. W., et al. (2001). Calibration of SeaWiFS. II. Vicarious techniques. *Applied Optics*, 40, 6701–6718.
- Eplee, R. E., Jr., Sun, J. -Q., Meister, G., Patt, F. S., Xiong, X., & McClain, R. C. (2011). Cross calibration of SeaWiFS and MODIS using on-orbit observations of the moon. *Applied Optics*, 50, 120–133.
- Esaías, W. E., Abott, M. R., Barton, I., Brown, O. B., Cambell, J. W., Carder, K. L., et al. (1998). An overview of MODIS capabilities for ocean science observations. *IEEE Transactions on Geoscience and Remote Sensing*, 36, 1250–1264.
- Fougnie, B., Bracco, G., Lafrance, B., Ruffel, C., Hagolle, O., & Tinel, C. (2007). PARASOL in-flight calibration and performance. *Applied Optics*, 22, 5435–5451.
- Fournier, G., & Forand, J. L. (1994). Analytical phase function for ocean water. In J. S. Jaffe (Ed.), *Ocean Optics XII. Proceedings SPIE*, 2258. (pp. 194–201).
- Fournier, G., & Jonas, M. (1999). Computer-based underwater imaging analyses. In G. Gilbert (Ed.), *Airborne and In-water Underwater Imaging. Proceedings SPIE*, 3761. (pp. 62–77).
- Frouin, R., Schindling, M., & Deschamps, P. -Y. (1996). Spectral reflectance of sea foam in the visible and near-infrared: In situ measurements and remote sensing applications. *Journal of Geophysical Research*, 101, 14361–14371.
- Gérard, B., Deuzé, J. -L., Herman, M., Kaufman, Y. J., Lallart, P., Oudard, C., et al. (2005). Comparisons between POLDER2 and MODIS/Terra aerosol retrievals over ocean. *Journal of Geophysical Research*, 110, D24211. doi:10.1029/2005JD006218.
- Gordon, H. R. (1989). Can the Lambert-Beer law be applied to the diffuse attenuation coefficient of ocean water? *Limnology and Oceanography*, 34(8), 1389–1409.
- Gordon, H. R., Brown, O. B., & Jacobs, M. M. (1975). Computed relationships between the inherent and apparent optical properties of a flat homogeneous ocean. *Applied Optics*, 14, 417–427.
- Gordon, H. R., & McCluney, W. R. (1975). Estimation of the depth of sun light penetration in the sea for remote sensing. *Applied Optics*, 14, 413–416.
- Haltrin, V. (2002). One-parameter two-term Henyey-Greenstein phase function for light scattering in seawater. *Applied Optics*, 41, 1022–1028.
- Hansen, J. E., & Travis, L. D. (1974). Light scattering in planetary atmospheres. *Space Science Reviews*, 16, 527–610.
- Harmel, T., & Chami, M. (2008). Invariance of polarized reflectance measured at the top of the atmosphere by PARASOL satellite instrument in the visible range with marine constituents in open ocean waters. *Optics Express*, 9, 6064–6080.
- Hasekamp, O. P., & Landgraf, J. (2005). Retrieval of aerosol properties over the ocean from multispectral single-viewing-angle measurements of intensity and polarization: Retrieval approach, information content, and sensitivity study. *Journal of Geophysical Research*, 110, doi:10.1029/2005JD006212.
- Hasekamp, O. P., Litvinov, P., & Butz, A. (2011). Aerosol properties over the ocean from PARASOL multi-angle photometric measurements. *Journal of Geophysical Research*, 116, D14204. doi:10.1029/2010JD015469.
- Henyey, L. C., & Greenstein, J. L. (1941). Diffuse radiation in the galaxy. *The Astrophysical Journal*, 93, 70–83.
- Herman, L., Deuzé, J. -L., Marchand, A., Roger, B., & Lallart, P. (2005). Aerosol remote sensing from POLDER/ADEOS over the ocean: Improved retrieval using a nonspherical particle model. *Journal of Geophysical Research*, 110, doi:10.1029/2004JD004798.
- Hovenier, J. W., van der Mee, C., & Domke, H. (2004). *Transfer of Polarized Light in Planetary Atmospheres – Basic Concepts and Practical Methods*. Berlin: Springer.
- Huot, Y., Morel, A., Twardowski, M. S., Stramski, D., & Reynolds, R. A. (2008). Particle optical backscattering along a chlorophyll gradient in the upper layer of the eastern South Pacific Ocean. *Biogeosciences*, 5, 495–507.
- Kawata, Y., & Yamazaki, A. (1998). Multiple scattering analysis of airborne POLDER image data over the sea. *IEEE Transactions on Geoscience and Remote Sensing*, 51, 51–60.
- Knobelspiesse, K., Cairns, B., Redemann, J., Bergstrom, R. W., & Stohl, A. (2011). Simultaneous retrieval of aerosol and cloud properties during the MILAGRO field campaign. *Atmospheric Chemistry and Physics*. doi:10.5194/acp-11-6245-2011.
- Koepeke, P. (1984). Effective reflectance of oceanic whitecaps. *Applied Optics*, 23, 1816–1842.
- Loisel, H., & Morel, A. (1998). Light scattering and chlorophyll concentration in case 1 waters: A reexamination. *Limnology and Oceanography*, 43, 847–858.
- Mishchenko, M. I., Cairns, B., Hansen, J. E., Travis, L. D., Burg, R., Kaufman, Y. J., et al. (2004). Monitoring of aerosol forcing of climate from space: Analysis of measurement requirements. *Journal of Quantitative Spectroscopy and Radiative Transfer*, 88, 149–161.
- Mishchenko, M. I., Cairns, B., Kopp, G., Schueler, C. F., Fafaul, B. A., Hansen, J. E., et al. (2007). Accurate monitoring of terrestrial aerosols and total solar irradiance: Introducing the Glory Mission. *Bulletin of the American Meteorological Society*, 88, 677–691.
- Mishchenko, M. I., & Travis, L. D. (1997). Satellite retrieval of aerosol properties over the ocean using polarization as well as intensity of reflected sunlight. *Journal of Geophysical Research*, 102, 16989–17013.
- Mishchenko, M. I., & Travis, L. D. (1997). Satellite retrieval of aerosol properties over the ocean using measurements of reflected sunlight: Effect of instrumental errors and aerosol absorption. *Journal of Geophysical Research*, 102, 13543–13553.
- Mishchenko, M. I., Travis, L. D., Kahn, R. A., & West, R. A. (1997). Modeling phase functions for dustlike tropospheric aerosols using a shape mixture of randomly oriented polydisperse spheroids. *Journal of Geophysical Research*, 102, 16831–16847.
- Mishchenko, M. I., Travis, L. D., & Laci, A. A. (2002). *Scattering, Absorption, and Emission of Light by Small Particles*. Cambridge: Cambridge University Press <http://www.giss.nasa.gov/~crim/books.html>
- Mishchenko, M. I., Travis, L. D., & Laci, A. A. (2006). *Multiple scattering of light by particles: Radiative transfer and coherent backscattering*. Cambridge, UK: Cambridge University Press.
- Mishchenko, M. I., Travis, L. D., & Macke, A. (2000). T-Matrix method and its applications. In M. I. Mishchenko, J. W. Hovenier, & L. D. Travis (Eds.), *Light Scattering by Nonspherical Particles* (pp. 147–172). San Diego: Academic Press.
- Mobley, C. D. (1994). *Light and Water*. Radiative transfer in natural waters. San Diego: Academic Press.
- Mobley, C. D., Sundman, L. K., & Boss, E. (2002). Phase function effects on oceanic light fields. *Applied Optics*, 41, 1035–1050.
- Molina, L. T., Madronich, S., Gaffney, J. S., Apel, E., de Foy, B., Fast, J., et al. (2010). An overview of the MILAGRO 2006 campaign: Mexico City emissions and their transport and transformation. *Atmospheric Chemistry and Physics*, 10, 8697–8760. doi:10.5194/acp-10-8697-2010.
- Moore, T. S., Campbell, J. W., & Dowell, M. D. (2009). A class-based approach to characterizing and mapping the uncertainty of the MODIS ocean chlorophyll product. *Remote Sensing of Environment*, 113(11), 2424–2430.

- Morel, A. (1973). Diffusion de la lumière par les eaux de mer: Résultats expérimentaux et approche théorique. *AGARD Lecture Series*, 61. (pp. 3.1.1–3.1.7) English translation (A. Morel, 1976: The scattering of light by sea water: experimental results and theoretical approach. Translated by George Halikas) available at www.obs-vlfr.fr/LOV/OMT/personnes/z_more_an/morel.php
- Morel, A. (1974). Optical properties of pure water and pure sea water. In N. G. Jerlov, & E. Steeman Nielsen (Eds.), *Optical Aspects of Oceanography* (pp. 1–24). New York: Academic Press.
- Morel, A. (1988). Optical modeling of the upper ocean in relation to its biogenous matter content (case 1 waters). *Journal of Geophysical Research*, 93, 10749–10768.
- Morel, A. (2009). Are the empirical relationships describing the bio-optical properties of case 1 waters consistent and internally compatible? *Journal of Geophysical Research*, 114, C01016. doi:10.1029/2008JC004803.
- Morel, A., Antoine, D., & Gentili, B. (2002). Bidirectional reflectances of oceanic waters: Accounting for Raman emission and varying particle scattering phase function. *Applied Optics*, 41, 7058–7067.
- Morel, A., Claustre, H., Antoine, D., & Gentili, B. (2007). Natural variability of bio-optical properties in Case 1 waters: Attenuation and reflectance within the visible and near-UV spectral domains, as observed in South Pacific and Mediterranean waters. *Biogeosciences*, 4, 913–925.
- Morel, A., & Gentili, B. (1991). Diffuse reflectance of oceanic waters: Its dependence on sun angle as influenced by the molecular scattering contribution. *Applied Optics*, 30, 4427–4438.
- Morel, A., & Gentili, B. (2004). Radiation transport within oceanic (case 1) waters. *Journal of Geophysical Research*, 109, C06008. doi:10.1029/2003JC002259.
- Morel, A., & Gentili, B. (2009). A simple band ratio technique to quantify the colored dissolved and detrital organic material from ocean color remotely sensed data. *Remote Sensing of Environment*. doi:10.1016/j.rse.2009.01.008.
- Morel, A., & Maritorena, S. (2001). Bio-optical properties of oceanic waters: A reappraisal. *Journal of Geophysical Research*, 106, 7163–7180.
- Morel, A., & Prieur, I. (1977). Analysis of variations in ocean color. *Limnology and Oceanography*, 22, 709–722.
- Nelson, N. B., & Siegel, D. A. (2002). Chromophoric DOM in the open ocean. In D. A. Hansell, & C. A. Carlson (Eds.), *Biogeochemistry of Marine Dissolved Organic Matter* (pp. 547–578). San Diego: Academic Press.
- Nobileau, N., & Antoine, D. (2005). Detection of blue-absorbing aerosols using near infrared and visible (ocean color) remote sensing observations. *Remote Sensing of Environment*, 95, 378–387.
- Peralta, R. J., Nardelli, C., Cairns, B., Russell, E. E., Travis, L. D., Mishchenko, M. I., et al. (2007). Aerosol Polarimetry Sensor for the Glory Mission. *Proceedings of SPIE*, 6786, 67865L.
- Pope, R. M., & Fry, E. S. (1997). Absorption spectrum (380–700 nm) of pure water. II. Integration cavity measurements. *Applied Optics*, 36, 8710–8723.
- Redemann, J., Zhang, Q., Livingston, J., Russel, P., Shinozuka, Y., Clarke, A., et al. (2009). Testing aerosol properties in MODIS Collection 4 and 5 using airborne sunphotometer observations in INTEX-B/MILAGRO. *Atmospheric Chemistry and Physics*, 9, 8159–8172.
- Sancer, M. I. (1969). Shadow-corrected electromagnetic scattering from a randomly rough ocean surface. *IEEE Transactions on Antennas and Propagation*, 17, 557–585.
- Siegel, D. A., Maritorena, S., Nelson, N. B., Hansell, D. A., & Lorenzi-Kayser, M. (2002). Global distribution and dynamics of colored dissolved and detrital organic materials. *Journal of Geophysical Research*, 107(C12), 3228. doi:10.1029/2001JC000965.
- Smith, R. C., & Baker, K. S. (1981). Optical properties of the clearest natural waters (200–800 nm). *Applied Optics*, 20, 177–184.
- Stramski, D., Boss, E., Bogucki, D., & Voss, K. J. (2004). The role of seawater constituents in light backscattering in the ocean. *Progress in Oceanography*, 61, 27–56.
- Stramski, D., & Kiefer, D. A. (1991). Light scattering by microorganisms in the open ocean. *Progress in Oceanography*, 28, 343–383.
- Stramski, D., & Woźniak, S. B. (2005). On the role of colloidal particles in light scattering in the ocean. *Limnology and Oceanography*, 50, 1581–1591.
- Twardowski, M. S., Boss, E., Macdonald, J. B., Pegau, W. S., Barnard, A. H., & Zaneveld, J. (2001). A model for estimating bulk refractive index from the optical backscattering ratio and the implications for understanding particle composition in case I and case II waters. *Journal of Geophysical Research*, 106(C6), 14129–14142.
- Ulaby, F. T., & Elachi, C. (Eds.). (1990). *Radar Polarimetry for Geoscience Applications*. Norwood, MA: Artech House.
- van de Hulst, H. C. (1980). *Multiple Light Scattering. Tables, Formulas, and Applications*. San Diego: Academic Press.
- Videen, G., Yatskiv, Ya, & Mishchenko, M. (Eds.). (2004). *Photopolarimetry in Remote Sensing*. Berlin: Springer.
- Voss, K. J., & Fry, E. S. (1984). Measurements of the Mueller matrix for ocean water. *Applied Optics*, 23, 4427–4439.
- Voss, K. J., Gleason, A. C. R., Gordon, H. R., Kattawar, G. W., & You, Y. (2011). Observation of non-principal plane neutral points in the in-water polarized light field. *Optics Express*, 17, 5942–5952.
- Woźniak, S. B., & Stramski, D. (2004). Modeling the optical properties of mineral particles suspended in seawater and their influence on ocean reflectance and chlorophyll estimation from remote sensing algorithms. *Applied Optics*, 43, 3489–3503.
- Zaneveld, J. R., Roach, D. M., & Pak, H. (1974). The determination of the index of refraction distribution of oceanic particles. *Journal of Geophysical Research*, 79, 4091–4095.
- Zhai, P., -W., Hu, Y., Chowdhary, J., Trepte, C. R., Lucker, P. L., & Josset, D. B. (2010). A vector radiative transfer model for coupled atmosphere and ocean systems with a rough interface. *Journal of Quantitative Spectroscopy and Radiative Transfer*, 111, 1025–1040.